Applied Ocean Research 170 (2026) 105032

Contents lists available at ScienceDirect

Applied Ocean Research

journal homepage: www.elsevier.com/locate/apor

Research paper

Flow field around *Coandă effect*-based polymetallic-nodule collector: Insights from three-dimensional numerical simulations

Lalit Kumar [a,b], Sebastiaan Mulders [b], Said Alhaddad [a,*]

[a] Department of Maritime and Transport Technology, Faculty of Mechanical Engineering, Delft University of Technology, Mekelweg 2, Delft, 2628 CD, The Netherlands

[b] Delft Center for Systems and Control, Faculty of Mechanical Engineering, Delft University of Technology, Mekelweg 2, Delft, 2628 CD, The Netherlands

ARTICLE INFO

Keywords:
Deep sea mining
Polymetallic nodules
Coandă-effect
Wall-attached jet
Water entrainment

ABSTRACT

Recent advancements have demonstrated that collectors based on the Coandă effect can effectively harvest polymetallic nodules from the seabed. However, the hydrodynamics of the flow around such collectors, particularly the mechanisms of ambient water entrainment, remain insufficiently explored. To address this gap, we performed three-dimensional numerical simulations to investigate the flow characteristics surrounding a *Coandă effect*-based collector, focusing on the effects of main jet velocity, secondary jet velocity, radius of curvature, and bottom clearance. The results show that increasing the main jet velocity enhances flow attachment and strengthens the pressure gradients beneath the collector, thereby increasing the entrainment of ambient water into the collection duct. Similarly, higher secondary jet velocities improve flow attachment and raise the collection duct flow rate but also lead to greater sideways water spillage. Furthermore, a larger radius of curvature reduces sideways spillage, consequently promoting greater ambient water entrainment beneath the collector. Likewise, increasing the bottom clearance enhances ambient water entrainment. Overall, these findings provide valuable insights for optimizing the operational parameters of *Coandă effect*-based collectors to maximize collection efficiency while minimizing water spillage.

1. Introduction

The need for mineral resources has increased in recent years due to the rapid development of civilization. As terrestrial reserves rapidly deplete, the search for alternatives has shifted towards the deep-sea ocean (Toro et al., 2020). This transition is mainly driven by the demand for critical metals such as manganese, cobalt, nickel, and copper, which has accelerated the development of deep-sea mining technologies. Such metals are abundantly present in polymetallic nodules discovered at the seabed, and these are essential for the creation of advanced technology like electronics, smartphones, and electric cars. However, mining these nodules has environmental consequences, including disturbance of seabed sediments, which poses a threat to the marine ecosystem (Amudha et al., 2024; Q. Zhang et al., 2024).

Numerous studies have examined the practicality and economic feasibility of mining polymetallic nodules from the deep sea (Boetius and Haeckel, 2018; Elerian et al., 2021). The extraction of these nodules generally employs mechanical, hydraulic, or hybrid techniques (Min et al., 1997), among these, hydraulic methods are the most popular due to their high collection efficiency and lower environmental impact. Generally, hydraulic collectors are divided into two types: (i) wall-attached jet and (ii) double-drainage jet flushing collector (Jia et al., 2023; Yue et al., 2021a; Zhao et al., 2021). The wall-attached jet collector is preferred over the double-drainage jet flushing collector, because it gently lifts the nodules, rather than pushing them with strong water jets. The wall-attached jet collector, also referred to as the *Coandă effect*-based collector, guides the nodules smoothly into the collection duct. However, the nodules are lifted by front and rear jet flows in the double-row hydraulic sluicing method (Yue et al., 2021). Recent developments in the *Coandă effect*-based collector (Lee et al., 2013; Alhaddad et al., 2023), are intended to improve cost-effectiveness and easy operation, while reducing environmental impacts (Hao and di Mare, 2023; Mao et al., 2024).

The term *Coandă effect* was introduced by the Romanian physicist Henri Coandă. This phenomenon refers to the tendency of fluid particles to adhere to a solid boundary, a property that plays an important role in nodule collection. The collector generates a high-speed jet flow, creating a pressure difference between the seabed and a curved plate, which lifts nodules from the seabed (Kim et al., 2018). Subsequently, the nodules are drawn into the collection duct by the suction generated

* Corresponding author.
E-mail address: S.M.S.Alhaddad@tudelft.nl (S. Alhaddad).

https://doi.org/10.1016/j.apor.2026.105032
Received 5 November 2025; Received in revised form 3 February 2026; Accepted 13 March 2026
Available online 16 March 2026

by the fast-moving water jet along the curved surface. Unlike traditional hydraulic collectors, designs based on the *Coandă effect* reduce sediment resuspension by directing the jet flow along the contour of a specially adapted curved base plate. This regulated flow decreases turbulence inside the collector head, improving pick-up efficiency while minimizing environmental disturbance (Alhaddad and Helmons, 2023).

The flow field beneath the *Coandă effect*-based collector has been investigated in a limited number of studies. Rodman et al. (1989) conducted jet experiments to study the impact of curved-wall jet curvature on flow fields. The authors proposed a semi-theoretical and semi-empirical technique for analyzing velocity and pressure distributions. Further, Kim et al. (2018) studied the effect of the jet impinging angle and Reynolds number with a constant distance from nozzle-to-surface distance of the circular cylinder. The authors observed that increasing the impinging angle of the jet enhances the momentum of the jet as it leaves the nozzle, causing the wall jet to adhere longer to the cylinder surface and shifting the flow separation point downstream at a given Reynolds number. Zhao et al. (2021) studied the flow field behavior beneath the collector using PIV measurements. The authors observed that the *Coandă effect*-based method requires lower flow rates but induces greater flow field disturbances, whereas the suction method offers flow field stability at higher energy costs.

In terms of collector design and performance, Cho et al. (2019) developed a collector prototype mounted on a crawler to examine its performance for manganese collection. The authors observed that the water flow rate through the nozzle, radius of the nozzle, radius of the attached plate, clearance, and track length are essential design components for nodule collection. Further, Hu et al. (2020) studied the suck-up-based and Coandă-effect-based devices using 3D printed models and particle image velocimetry (PIV) technology. The authors observed that the velocity change in the vortex region developed at the sphere's top improves the collection efficiency and reduces bottom disturbances in the *Coandă effect*-based collector. Yue et al. (2021) conducted experiments and numerical simulations comparing suck-up-based, *Coandă effect*-based, and double-row hydraulic sluicing collectors. The *Coandă effect*-based collectors outperformed the others in terms of energy efficiency and reduced flow field disturbance. B. Zhang et al. (2024) used a computational fluid dynamics–discrete element method (CFD-DEM) to examine the flow field and collection efficiency. The authors also provided a design method for a wall-jet nodule collection device that adjusts its geometric shape to produce a flow field that makes it easy to start nodule collection while keeping the flow velocity in the near-bottom region low.

Alhaddad and Helmons (2023) conducted small-scale experiments to quantify sediment erosion by a *Coandă effect*-based collector. The authors observed that increased jet velocity and decreased collector velocity enhance erosion depth, while reducing the clearance between the collector and the bed results in stronger interaction between the jet flow and the sediment surface, leading to greater erosion depths. Further, the study also utilizes secondary jets along with the main jet flow to enhance the *Coandă effect* and regulate the flow field inside the collection duct. This not only improves nodule transport efficiency but also minimizes sediment resuspension and ambient water entrainment (Li et al., 2023; Jia et al., 2023). Furthermore, Alhaddad et al. (2023) utilized 2D CFD simulations to create an efficient design for a *Coandă effect*-based collector. Their design achieved high nodule pick-up efficiency with little disturbance to the seabed sediment. The authors also performed full-scale experiments and found that greater forward velocity decreases collection efficiency because the collector lacks adequate time to capture the nodules effectively. However, increasing the jet velocity increases the efficiency of nodule pick-up. The continuation of this research is evident in the study of Alhaddad et al. (2024), which provides a quantitative dataset on cohesive sediment erosion and turbidity currents from a moving *Coandă effect*-based collector. Their findings reveal a logarithmic relationship between erosion depth and flow impinging force applied on the clayey bed, while higher flow in the collection duct reduces the velocity of turbidity currents. These insights are valuable for enhancing erosion predictions and optimizing collector operations to minimize sediment plumes.

Using a theoretical model of curved wall jets, Jia et al. (2022) predicted the lift index (defined as the ratio of lift force to nodule weight), and found that higher jet velocity and greater jet duct height enhance the *Coandă effect*. By minimizing the need for extensive prototyping, this theoretical framework optimizes the design of nodule collectors based on the *Coandă effect*. Furthermore, Jia et al. (2023) examined the flow field underneath the collector to evaluate lift capabilities while studying jet flow on logarithmic spiral surfaces. The results indicate that although the jet growth rate increases with downstream distance, lift is enhanced by higher jet velocity, local curvature, and jet duct height. Further, Jia et al. (2024) explored the impact of curvature radius on a *Coandă effect*-based collector using CFD-DEM. The curved jet entrains seawater, preventing erosion and generating lift through pressure gradients and jet energy. A higher curvature radius increases jet diffusion but reduces collection efficiency.

The above-mentioned literature on experimental, numerical, and theoretical studies on *Coandă effect*-based collectors have mainly focused on jet attachment behavior, lift force or lift index, collection efficiency, and sediment erosion. Several works have examined the effects of jet velocity, curvature radius, and clearance on nodule pick-up performance and seabed disturbance. The available literature shows that seabed disturbances are largely controlled by the flow around the collector, which governs sediment transport (Alhaddad and Helmons, 2023; Li et al., 2024), plume generation (Wu et al., 2025; Li et al., 2025), turbidity current formation (Stoffers et al., 2024; Alhaddad et al., 2024), and particle flocculation (Peacock and Ouillon, 2023).

Despite these advances, the ambient-water entrainment has not been directly quantified, nor has its dependence on collector geometry and operating conditions been systematically examined, particularly in three-dimensional flow fields. Moreover, a detailed analysis of the flow hydrodynamics, including the distinction between ambient water entering the collection duct and water spillage from the collector, have not been quantified. To address these gaps, the present study uses three-dimensional numerical simulations to investigate the flow hydrodynamics and to quantify ambient-water entrainment around a *Coandă effect*-based collector. It systematically examines the effects of jet configuration, jet velocity, plate curvature radius, and bottom clearance on flow behavior and entrainment, providing new insights and practical guidance for optimizing collector design and operating conditions. The main contributions of this work are:

1. Investigation of flow behavior around single-jet and double-jet configurations, providing new insights into their hydrodynamics, including differences in ambient water entrainment and water spillage around the collector.
2. Examination of the impact of jet velocities on the flow attachment, pressure gradient development, and the resulting ambient water entrainment.
3. Evaluation of the effects of plate curvature radius and bottom clearance on the flow rate in the collection duct, of the ambient water entrainment and spillage.

This paper is structured as follows. Section 2 outlines the methodology, including the *Coandă effect*-based collector, its design parameters, and the three-dimensional numerical modeling framework. Section 3 presents the numerical results and discusses the findings, focusing on the flow field characteristics and water entrainment behavior beneath the collector. Section 4 summarizes the main conclusions of the study. Finally, Section 5 presents limitations and directions for future research.

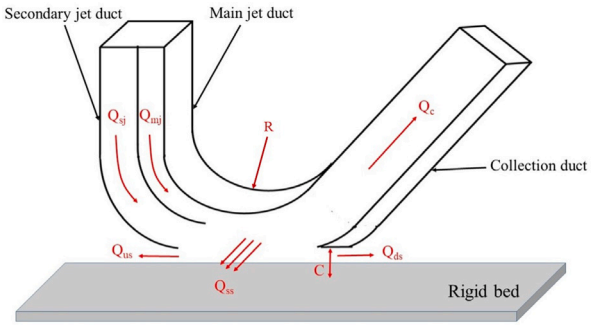

Fig. 1. A schematic diagram of the *Coandă effect*-based hydraulic collector, where C is the bottom clearance between collector and rigid bed and R is the upper plate's radius of curvature. Q_{mj} and Q_{sj} represent the volumetric flow rates in the main jet duct and secondary jet duct, respectively. Q_c is the volumetric flow rate in the collection duct. Q_{us}, Q_{ds}, and Q_{ss} represent the upstream, downstream, and sideways spillage, respectively.

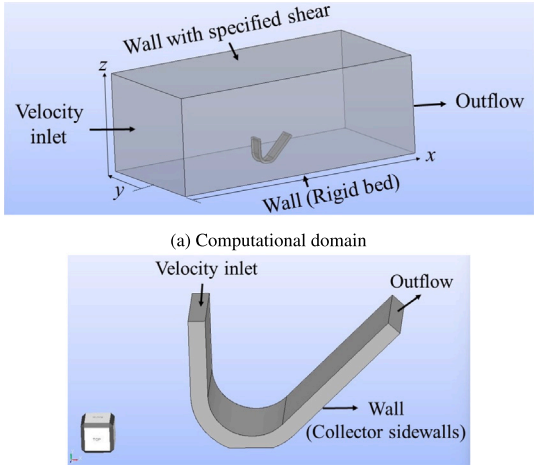

(a) Computational domain

(b) *Coandă effect*-based hydraulic polymetallic nodule collector

Fig. 2. Boundary conditions for (a) the computational domain and (b) the collector. In (a), the computational domain is defined with a velocity inlet on the left side, an outflow condition on the right side, a rigid bed at the bottom, and a top wall modeled as a wall with a zero shear stress to represent the free surface. In (b), the collector geometry is shown with jet ducts as velocity inlets, the collector outlet defined as outflow, and solid walls representing the collector sidewalls.

2. Methodology

This section describes the *Coandă effect*-based collector design, along with the computational Fluid Dynamics (CFD) approach used to model the three-dimensional flow field around the collector. It includes the numerical modeling techniques, the boundary conditions applied to the computational domain and the collector, mesh generation, and validation studies to ensure the accuracy and reliability of the numerical results.

This study uses the collector design introduced by Alhaddad and Helmons (2023) to explore the flow dynamics. Fig. 1 presents a schematic of the basic design of the collector, comprising four surfaces that form three ducts: the main jet duct, the secondary jet duct, and the collection duct. The bottom clearance (C) is defined as the vertical distance beneath the rear cowl of the collection duct, whereas R represents the radius of curvature of the collector's upper plate. In this configuration, the high-velocity flow in the main jet duct (Q_{mj}) follows the curvature of the upper plate due to the *Coandă effect*, allowing it to remain attached to the surface. Due to the development of a pressure gradient under the collector, the surrounding water is drawn into the collector, creating a suction effect that lifts seabed polymetallic nodules and transports them towards the collection duct (Q_c). This causes water spillage downstream (Q_{ds}), upstream (Q_{us}) and sideways (Q_{ss}) of the collector, as will be presented later in this study.

2.1. Three-dimensional (3D) numerical modeling

To examine the flow hydrodynamics around the collector, a three-dimensional computational fluid dynamics (CFD) modeling is performed using ANSYS Fluent. This solver simulates fluid flow problems by solving the Navier–Stokes equations (Pan et al., 2024). The Finite Volume Method (FVM) is utilized to discretize the computational domain into smaller control volumes. Further, the governing equations are solved iteratively within each volume. ANSYS Fluent computes key flow parameters such as velocity, pressure, density, and volume fraction at the centroids of these control volumes. The iteration continues until the solution converges, ensuring that flow properties are conserved and the specified boundary conditions are satisfied.

In the present numerical model, the k-ω SST turbulence model was employed to simulate turbulence, as it offers high accuracy in capturing boundary layer effects and flow separation zones (Coughtrie et al., 2013). For pressure-velocity coupling, the SIMPLE (Semi-Implicit Method for Pressure Linked Equations) scheme was employed. Spatial discretization was carried out using second-order accurate schemes to ensure higher fidelity in capturing flow gradients, while a second-order implicit scheme was used for time advancement to maintain stability and accuracy in transient simulations. The scaled residual convergence criteria for the governing equations (continuity, momentum, k, and ω) were set to 10^{-4}, 10^{-7}, 10^{-6}, and 10^{-6}, respectively. A fixed time-step size of 0.00325 s was used for all numerical simulations. The numerical setup was also tested with a smaller time-step size, which showed no differences in the monitored flow variables, thereby confirming time-step independence. During the simulations, flow variables such as velocity and pressure were continuously monitored. Convergence was achieved after approximately 2000 time steps, with 22 iterations per time step. To ensure solution stability and robustness, the simulations were extended to 2400 time steps.

2.2. Boundary conditions

The computational domain used in this study is shown in Fig. 2, in which the boundary conditions used for (a) the computational domain and (b) the collector are illustrated. In Fig. 2(a), the computational domain is defined with a velocity inlet on the left side, an outflow condition on the right side, a rigid bed at the bottom, and a top wall modeled as a wall with a zero shear stress to represent the free surface. In Fig. 2(b), the collector geometry is shown with jet ducts as velocity inlets, the collector outlet defined as outflow, and solid walls representing the collector sidewalls. These boundary conditions were applied to each side of the computational domain to accurately replicate the physical conditions of the available experiments, which were used for validation purposes. The rigid bed was modeled as a no-slip wall boundary condition to accurately simulate the resistance offered by the rigid bed to fluid flow.

2.3. Mesh generation

The present study employs an unstructured mesh configuration composed of quadrilateral elements to discretize the water surface within the computational domain, offering greater flexibility for representing the complex geometry of the collector compared to structured meshes. The unstructured elements allow for localized refinement (smaller mesh) around regions of high velocity gradients, and a coarse

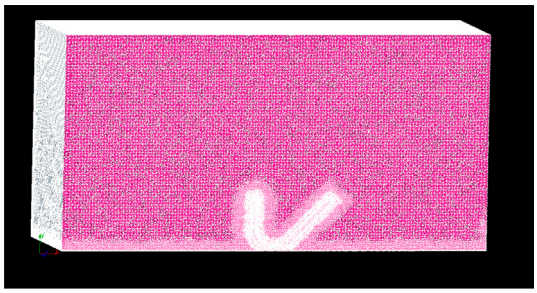

(a) 3D unstructured mesh in the computational domain

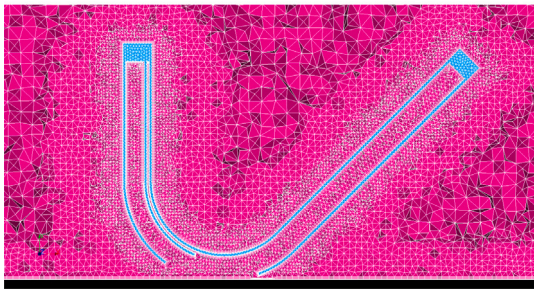

(b) Boundary layer elements for the mesh at collector

Fig. 3. 3D mesh in the computational domain, where (a) shows the overall unstructured 3D mesh used to capture the flow field around the collector, ensuring adequate resolution in the domain, and (b) highlights the prism layers near the collector, which are refined to accurately resolve velocity gradients and near-wall effects.

mesh size is used in less critical regions, which helps in improving computational efficiency. Further, the prism layers were also employed at the solid surface of the collector and rigid bed to effectively capture the boundary layer flow behavior since flow gradients are steep near solid walls and require fine resolution normal to the surface for adequate representation.

The computational domain meshes were generated using Salome, an open-source platform (Lande, 2021; Michelsen et al., 2012) well-suited for generating unstructured meshes around complex curved geometries. The three-dimensional unstructured mesh within the computational domain is shown in Fig. 3(a). Further, Fig. 3(b) represents the boundary layer elements of the mesh with a visible prism layer, at the collector sidewalls and the rigid bed.

2.4. Model validation

The numerical model is first validated against the experimental dataset of Suleman (2023), which reports a series of experiments on the interaction of a *Coandă effect*-based collector with a rigid bed. Suleman (2023) utilized the collector head introduced in Alhaddad and Helmons (2023). The collector was installed in the center of the flume, ensuring a constant bottom clearance of 18 mm from the bed surface. The flume width was 0.4 m, and the water depth was maintained at 37 cm. A series of small-scale tests were performed by varying the main jet velocity (V_{mj}) at 2.0, 3.0, and 4.4 m/s, while the secondary jet velocity was kept constant at zero. An electromagnetic flow meter (EMF) working with ±1% of accuracy mounted at the collector outlet measured corresponding collector outflow velocities (V_c) of 0.09, 0.36, and 0.51 m/s, respectively.

For validation, the computational domain was designed to represent the same laboratory-scale environment, and the simulations were carried out under identical conditions, using the same hydraulic parameters as described in Suleman (2023). Similar to the experiments, the main jet velocity V_{mj} was varied between 2.0, 3.0, and 4.4 m/s. The

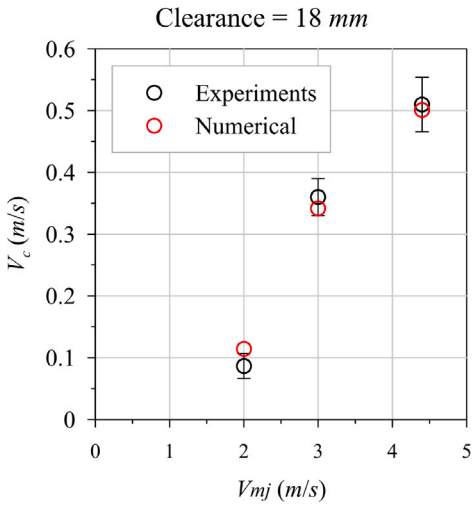

Fig. 4. Comparison of experimental and numerical results for the flow velocity through the collection duct with respect to the main jet velocity for a clearance of 18 mm. A good agreement between the numerical model and experimental data is observed, indicating that the simulation accurately captures the flow hydrodynamics around the collector.

corresponding velocities achieved in the collection duct V_c obtained from the simulations were 0.11, 0.34, and 0.50 m/s, respectively. The comparison of the experimental and numerical results is shown in Fig. 4, where very good agreement is observed, confirming the accuracy and reliability of the present numerical model. The results show an increase in collection duct velocity V_c corresponding to the main jet velocity V_{mj}.

The numerical model is also validated for the velocity profiles underneath and downstream of the collector (0.25 m away from the center of the collector) with the experimental findings of Alhaddad et al. (2023). In the experiments, a primary jet flow velocity of 4 m/s and a secondary jet velocity of 0.75 m/s were provided with a bottom clearance of 7.5 mm. Additionally, a collection duct velocity of 1.16 m/s was imposed. Considering the same hydraulic parameters, a numerical simulation was performed using the present CFD model. The velocity profiles are retrieved at two locations, marked as locations A and B, shown in Fig. 5(a). Location A was placed in a confined downstream area where the flow accelerates due to the collector sidewalls and the rigid bed. Although the geometry is narrow, this location is suitable for checking the downstream flow consistency and ensuring correct outflow development in the model. Further, location B was positioned outside the collection region to evaluate the flow velocity and to confirm that the numerical results capture the water spillage accurately.

The comparison plot of the velocity profile at location A is shown in Fig. 5(b). It can be observed that the numerical results of the velocity profile closely match the experimental data of Alhaddad et al. (2023). However, a relatively larger discrepancy between the experimental and numerical velocities is observed in the region 1–4 mm above the bottom wall. This zone corresponds to the near wall boundary layer, where the flow is strongly affected by steep velocity gradients, surface roughness effects, and local pressure variations. Such near wall dynamics are highly sensitive to small geometric or surface irregularities, which can amplify measurement uncertainty in experiments (Spalart and Watmuff, 1993). In the numerical model, the use of a RANS formulation with the k-ω SST turbulence model limits the ability to fully resolve the fine-scale structure of the boundary layer, particularly in regions of strong shear (Menter, 1994; Wilcox et al., 1998). These combined factors contribute to the relatively larger error observed in this narrow near-wall region.

Despite this localized deviation, the result shows good agreement between the numerical and experimental velocity profiles remains

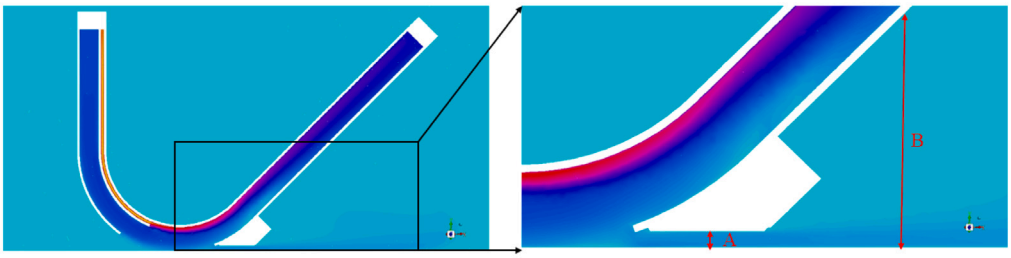

(a) Locations A and B at which velocity profiles are obtained.

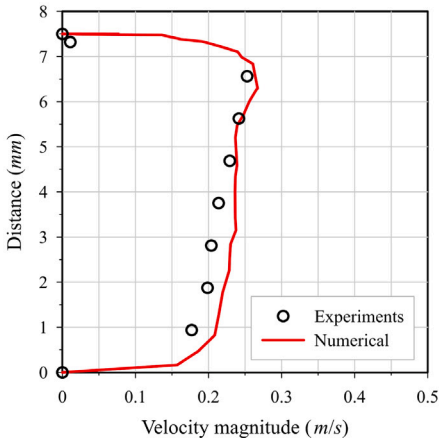

(b) Experimental and numerical velocity profiles at location A

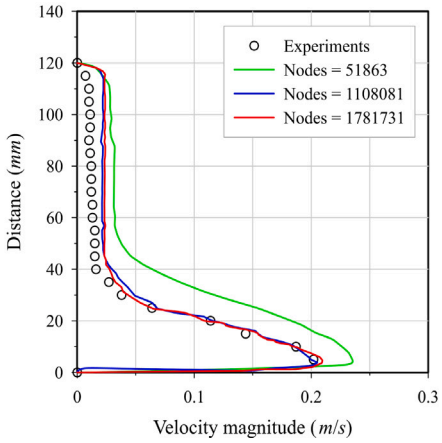

(c) Experimental and numerical velocity profiles at location B

Fig. 5. (a) Locations of extracted velocity profiles (b) Validation of the velocity profile at location A, demonstrating close agreement between experimental data and numerical simulation (c) Validation of the velocity profile at location B, including a mesh convergence study; results indicate that the medium (1108081 Nodes) and fine meshes (1781731 Nodes) yield nearly identical velocity profiles and closely match experimental data, confirming grid independence and reliable model accuracy.

strong, indicated by statistical metrics. These yield a low root mean square error ($RMSE$) of 0.149, a mean absolute error (MAE) of 0.02021, and a high coefficient of determination (R^2) of 0.987. The low $RMSE$ and MAE indicate small average deviations between the numerical and experimental results, while the high R^2 value confirms that the numerical model accurately captures the measured velocity profiles. Further, the velocity profile at location B is also validated and used for the mesh size study in the following subsection.

2.5. Mesh dependency

The velocity profile at location B (marked in Fig. 5(a)) is also investigated with different numbers of nodes and compared with the experimental data (Fig. 5(c)). It can be observed that the velocities obtained using a coarse mesh (51,863 nodes) are larger than the experimental ones, indicating inadequate resolution. The statistical metrics indicate a relatively large $RMSE$ of 0.0493 and MAE of 0.0441, reflecting poor agreement with the experimental data, along with a low R^2 value of 0.622, which indicates weak predictive accuracy for the coarse mesh. As the mesh size is refined to a medium mesh (1,108,081 nodes), the numerical results of the velocity profile become much closer to the experimental data. The statistical metrics also indicate a relatively lower $RMSE$ of 0.0096 and MAE of 0.0074, reflecting good agreement with the experimental velocity data, along with a higher R^2 value of 0.972, which indicates better predictive accuracy than the coarse mesh.

Further refinement of the mesh (1,781,731 nodes) shows minimal variations in the velocity profile compared to the medium mesh, indicating numerical convergence. The statistical values also confirm this, with only small improvements in $RMSE$ (0.0079), MAE (0.0063), and R^2 (0.981). A higher R^2 value of 0.981 represents a stronger match between the numerical predictions and the experimental measurements of velocity profiles. Since the medium and fine mesh results are comparable, the medium mesh is adopted for all the numerical simulations in the present study. Based on the validation results, it can be observed that the developed numerical model is reliable and accurate. A sufficiently large computational domain of 3 m in length, 2 m in width, and 1.5 m in depth will be adopted in the present study to ensure that boundary effects, including free-surface influence and lateral confinement, remain minimal in the region of interest around the collector.

3. Results and discussion

This section presents numerical results and discusses the flow hydrodynamics around the collector, quantifying the ambient water entrainment and spillage. The ambient water entrainment (Q_{aw}) is defined as the total flow rate of the ambient water that ends up in the collection duct. The term 'spillage' refers to the portion of the supplied flow rate through the jet ducts that does not end up in the collection duct. The spilled water can flow in four directions – upstream, downstream, left, and right – with the lateral components (left and right) collectively termed sideways spillage. The flow rate of the net entrained ambient water into the collection duct can be calculated from the following continuity equation:

$$Q_{aw} = (Q_c + Q_{us} + Q_{ds} + Q_{ss}) - (Q_{mj} + Q_{sj}) \quad (1)$$

where Q_c is the flow rate through the collection duct, Q_{us} is the upstream spillage, Q_{ds} is the downstream spillage and Q_{ss} is the sideways spillage.

The main jet velocity, secondary jet velocity, radius of curvature, and bottom clearance are the key parameters of the collector (B. Zhang

Table 1
A summary of numerical experiments with variation in hydraulic and geometric parameters.

Sim.#	Q_{mj} (l/s)	V_{mj} (m/s)	Q_{sj} (l/s)	V_{sj} (m/s)	C (mm)	R (mm)	h (mm)	Fr_{mj} (-)	Fr_{sj} (-)	Fr(-)	Q_c (l/s)	Inflow Q_{us} (l/s)	Outflow Q_{us} (l/s)	Q_{ds} (l/s)	Q_{ss} (l/s)	Q_{aw} (l/s)
1	3	3	NA	NA	7.5	125	40	13.54	NA	4.50	1.44	0.08	2.98	0.95	−0.48	1.80
2	4.4	4.4	NA	NA	7.5	125	40	19.86	NA	10.54	2.11	0.27	5.18	1.23	−0.79	3.05
3	5.8	5.8	NA	NA	7.5	125	40	26.18	NA	20.78	2.90	0.28	7.80	1.92	−0.92	5.63
4	3	3	0	0	7.5	125	40	13.54	0	3.13	1.02	0	2.30	0.62	−0.32	0.63
5	4.4	4.4	0	0	7.5	125	40	19.86	0	10.14	2.11	0	1.73	1.37	−0.52	0.29
6	5.8	5.8	0	0	7.5	125	40	26.18	0	17.26	2.80	0	4.66	1.45	−0.82	3.93
7	5.8	5.8	3	0.48	7.5	125	40	26.18	0.86	11.39	4.26	0.11	0.32	1.19	1.72	3.08
8	5.8	5.8	6	0.96	7.5	125	40	26.18	1.73	10.51	5.70	0.28	2.87	1.53	2.54	0.55
9	5.8	5.8	6	0.96	7.5	100	40	26.18	1.73	8.04	5.72	0.14	2.86	0.99	1.95	−0.40
10	5.8	5.8	6	0.96	7.5	150	40	26.18	1.73	11.60	5.69	0.15	2.88	1.18	2.60	0.40
11	5.8	5.8	6	0.96	13	125	45.5	26.18	1.73	12.64	5.69	0.12	2.23	2.02	2.92	0.94
12	5.8	5.8	6	0.96	18	125	50.5	26.18	1.73	17.73	5.69	0.54	1.62	2.65	3.64	1.26

Note: 'NA' represents the cases of a single-jet collector, where the secondary jet duct is not available.

et al., 2024; Alhaddad and Helmons, 2023). Therefore, we investigate the effect of these parameters on the ambient water entrainment and flow behavior. To this end, the velocity field, pressure field, and streamline patterns around the collector are analyzed. In total, a set of 12 numerical simulations was performed, and a summary of these simulations is given in Table 1, where h represents the vertical distance between the rigid bed and the lower point of the upper curved plate.

3.1. Effect of main jet flow velocity V_{mj}

To examine the effect of the main jet velocity, V_{mj} was systematically varied between 3.0, 4.4, and 5.8 m/s. The other parameters, such as the radius of curvature of the upper plate of the collector (R = 125 mm) and the bottom clearance (c = 7.5 mm), were kept constant. Since the results of Alhaddad et al. (2024) suggested that the presence of a secondary jet itself affects the flow hydrodynamics, we considered cases in which the secondary jet was absent (Simulations 1–3) and cases in which it was present but had a zero flow rate (Sim. 4–Sim. 6).

The results show that increased V_{mj} results in an increased velocity inside the collection duct (V_c), due to the larger supply of water and a stronger ambient water entrainment around the collector. For the single-jet collector (Sim. 3), the entrained water mainly entrains from the lower part of the upstream direction, which extends from the lower wall of the jet duct at the duct exit to the bed. However, no incoming ambient water is observed from the upstream direction in the double-jet collector (Sim. 6), as illustrated in Fig. 6. In this figure, positive x-velocity values represent incoming flow contributing to the system, while negative values indicate upstream spillage. Similar to Sim. 6, the x-component velocity profiles consistently indicate upstream spillage in Sim. 6–Sim. 12.

In addition to the upstream entrainment, ambient water is also drawn laterally into the system. The velocity profiles in the y-direction (Fig. 7) demonstrate that the collector entrains water from its lateral sides, which subsequently contributes to the flow underneath the collector. Positive y-velocity values correspond to incoming lateral flow, whereas negative values indicate sideways spillage. The results show that while both the single-jet and double-jet configurations entrain lateral water, the double-jet collector exhibits stronger sideways spillage compared to the single-jet case. This lateral spillage reduces the net inflow and indicates that a portion of the supplied water is spilled sideways rather than being directed into the collection duct. Similar to Sim. 6, the y-component velocity profiles consistently indicate sideways spillage in cases Sim. 6 to Sim. 12.

Further, the downstream velocity profiles for V_{mj} = 5.8 m/s (Fig. 8) show that no incoming flow is observed from the downstream direction for either the single-jet or double-jet collector. In both configurations, the flow is consistently running backward, indicating that the downstream region only experiences spillage and no entrainment. This behavior confirms that no water entrainment occurs in the downstream direction. This is consistently observed across all simulations performed in this study.

Fig. 9 presents the static pressure contours for different main jet velocities (V_{mj}) in both single-jet (Figs. 9(a)–9(c)) and double-jet (Figs. 9(d)–9(f)) configurations. In the single-jet configuration, under-pressure zone is observed at the main jet duct exit and near the upper

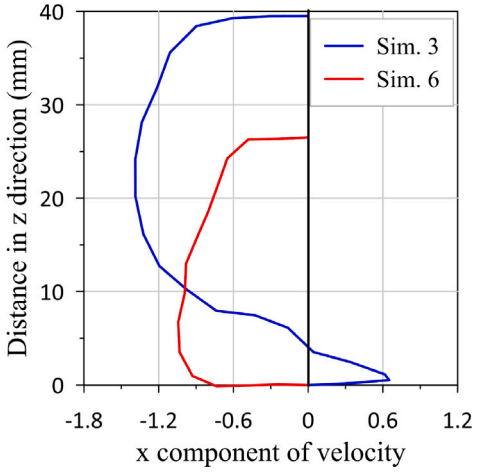

Fig. 6. Velocity profiles in the x-direction at the upstream section for the single-jet collector (Sim. 3) and the double-jet collector (Sim. 6). In the single-jet case, entrained water originates mainly from the lower bed upstream of the collector, while in the double-jet case no upstream inflow is observed. Positive x-velocity values denote incoming flow contributing to the system, whereas negative values indicate upstream spillage.

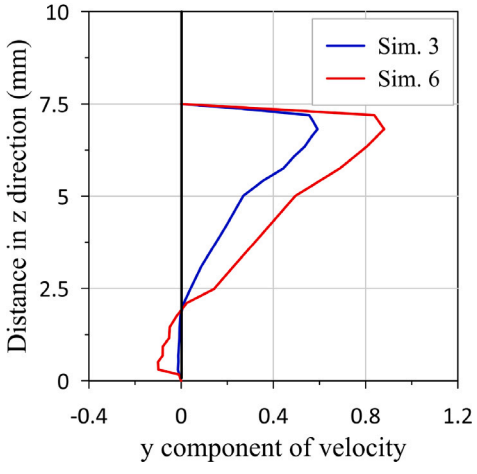

Fig. 7. Lateral velocity profiles in y-direction illustrating sideways entrainment and spillage for the single-jet collector (Sim. 3) and the double-jet collector (Sim. 6). Positive y-velocity values represent incoming ambient flow contributing beneath the collector, while negative values indicate sideways spillage away from the system. The results show that although both configurations entrain lateral flow, the double-jet collector exhibits stronger sideways spillage compared to the single-jet case.

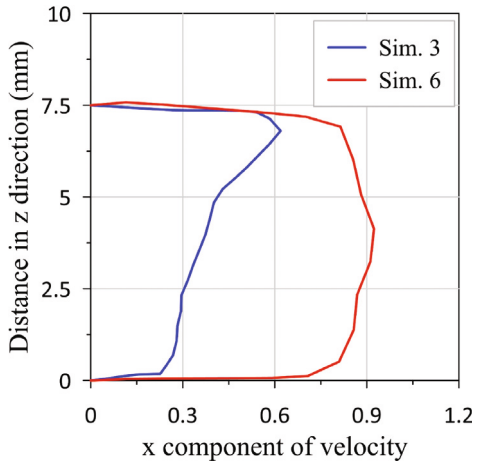

Fig. 8. Downstream velocity profiles for the single-jet (Sim. 3) and double-jet (Sim. 6) collectors at V_{mj} = 5.8 m/s. No incoming flow is observed from the downstream direction in either configuration.

curved surface of the collector (Figs. 9(a)–9(c)). However, the pressure at the rigid bed beneath the collector remains relatively higher in comparison to the pressure along the collector's upper curved plate. This pressure difference between the upper surface of the collector and the rigid bed establishes a vertical pressure gradient, which promotes the entrainment of ambient water into the collection duct. The effect becomes more pronounced with higher main jet velocity (Fig. 9(c)). Similar results of under pressures can be observed in the case of a double-jet collector, where the secondary jet duct has a zero velocity (Figs. 9(d)–9(f)). However, the magnitude of the under pressure is lower in the double-jet case compared to the single-jet configuration, resulting in a weaker suction effect and reduced ambient water entrainment in the double-jet collector. These observations are further supported by the variation of pressure drops (with respect to the ambient pressures) right under the collector along the *y*-axis for different V_{mj} in both single-jet and double-jet configurations, shown in Fig. 30 in the Appendix. All reported results in the present study, are time-averaged and correspond to quasi-steady-state flow conditions obtained after the numerical solution is fully converged. In the three-dimensional numerical simulations, flow variables such as velocity and pressure were continuously monitored and the convergence was confirmed.

Fig. 10 presents the velocity contours for varying main jet velocities (V_{mj}) in both single-jet (Figs. 10(a)–10(c)) and double-jet (Figs. 10(d)–10(f)) configurations. In a single-jet collector, the increase in the main jet velocity (3-5.58 m/s) leads to improved adherence of the flow to the upper curved plate of the collector. The term 'improved adherence' refers to the ability of the jet to remain attached to the upper curved plate over a longer arc length, with a delayed separation point. This interpretation is consistent with available literature (Kim et al., 2018), which shows that increased jet momentum enhances near-wall pressure gradients and shifts the detachment point downstream.

This adherence increases the velocity magnitude underneath the collector and results in a higher Q_c in the collection duct, as evident in Fig. 10(c). A similar trend is observed in the double-jet (V_{sj} = 0 m/s) configuration, where a higher Q_c is achieved for the case of V_{mj} = 5.8 m/s (Fig. 10(f)). This occurs mainly due to the increased water entrainment and suction effect generated by the high-speed jets. It can also be observed that the increase in the main jet velocity leads to an increase in spillage flow rates Q_{us} and Q_{ds}. This is because a larger main jet flow velocity induces a greater pressure drop beneath the collector, increasing the suction effect and drawing more surrounding water. However, in the case of the double-jet collector with V_{mj} = 3 m/s, the sideways spillage is evident (Table 1, Sim.# 4). This is mainly due to the smaller main jet velocity, which fails to generate a pressure drop comparable to that of Sim. #1. As a result, the jet diffuses laterally, resulting in sideways spillage and lower Q_c.

Fig. 11 presents a close-up of the velocity vector fields for different main jet velocities (V_{mj}) in single-jet (Figs. 11(a)–11(c)) and double-jet (Figs. 11(d)–11(f)) configurations. It can be observed that the flow behavior does not change significantly. However, the magnitude of velocity increases in the upstream, downstream, and the collection duct in both single-jet and double-jet collectors. The double-jet collector exhibits a lower velocity magnitude in the flow field compared to the single-jet collector, primarily due to the presence of the zero-velocity secondary jet duct towards which the recirculated water flow. These observations are further supported by the streamline plots presented in Fig. 34 in the Appendix.

Fig. 12 shows the velocity profiles underneath the collector for both single-jet (dashed lines) and double-jet (solid lines) configurations. In the near-bottom region (h = 0–20 mm), small negative x-velocity components are observed due to flow recirculation in both configurations. The velocity is zero at mid-height and peaks at h = 35 mm, and then decreases to zero at h = 40 mm owing to the solid boundary. As V_{mj} increases, the flow velocities under the collector rise significantly due to the larger backflow, reflecting stronger recirculation. This trend is consistent across both configurations, with higher V_{mj} producing more pronounced recirculation zones beneath the collector.

Fig. 13 presents the effect of Q_{mj} on the flow rates in and around the collector (i.e., Q_c, Q_{us}, Q_{ds}, Q_{aw}, and Q_{ss}). As shown in Fig. 13(a), Q_c increases with Q_{mj} in both configurations due to the enhanced *Coandă effect* (Alhaddad et al., 2023). The double-jet configuration exhibits slightly lower values, mainly because the secondary jet duct is inactive (zero velocity), which induces fluid movement into it due to backflow when the water separates from the upper curved surface. Fig. 13(b) shows that the single-jet collector has more upstream spillage compared to the double-jet configuration, because the absence of a secondary jet slot reduces flow confinement and allows more ambient water to escape upstream. Higher Q_{us} values are observed for larger main jet velocity in both configurations. Similarly, the increase in Q_{mj} leads to higher Q_{ds} (Fig. 13(c)). It can be observed that the flow from the sides contributes to the system in the single-jet collector due to the larger pressure difference. A similar contribution from the side flows is observed in the double-jet configuration for Q_{mj} = 3 and 4.4 m/s. At a higher main jet velocity (Q_{mj} = 5.8 m/s) in the double-jet configuration, sideways spillage becomes significant. Using the continuity equation (Eq. (1)), the net ambient water entrainment Q_{as} is computed for varying Q_{mj}, shown in Fig. 13(d). It can be observed that the rise in Q_{mj} leads to an increase in Q_{aw}.

3.2. Effect of secondary jet velocity

The secondary jet velocity (V_{sj}) was systematically varied to 0, 0.48, and 0.96 m/s, while the main jet velocity (V_{mj}) was fixed at 5.8 m/s. The radius of curvature of the collector's upper plate (R = 125 mm) and the bottom clearance (C = 7.5 mm) were also kept constant.

Fig. 14 presents the static pressure contours for varying secondary jet velocities (V_{sj}) in a double-jet configuration. When V_{sj} = 0 m/s, a larger under-pressure region develops near the main jet attachment zone, producing strong suction and enhanced entrainment from the ambient flow. As the secondary jet velocity increases (V_{sj} = 0.48 m/s), this under-pressure region gradually decreases and spreads more uniformly along the underside of the collector. At the highest secondary jet velocity V_{sj} = 0.96 m/s), the contours indicate a significant reduction in the magnitude of under pressure, resulting in lesser net ambient water entrainment (Table 1, Sim. # 8), which is consistent with the findings of Alhaddad et al. (2024). These observations are further supported by the variation of the pressure drop just under the collector's plate for double-jet configurations, shown in Fig. 31 in the Appendix.

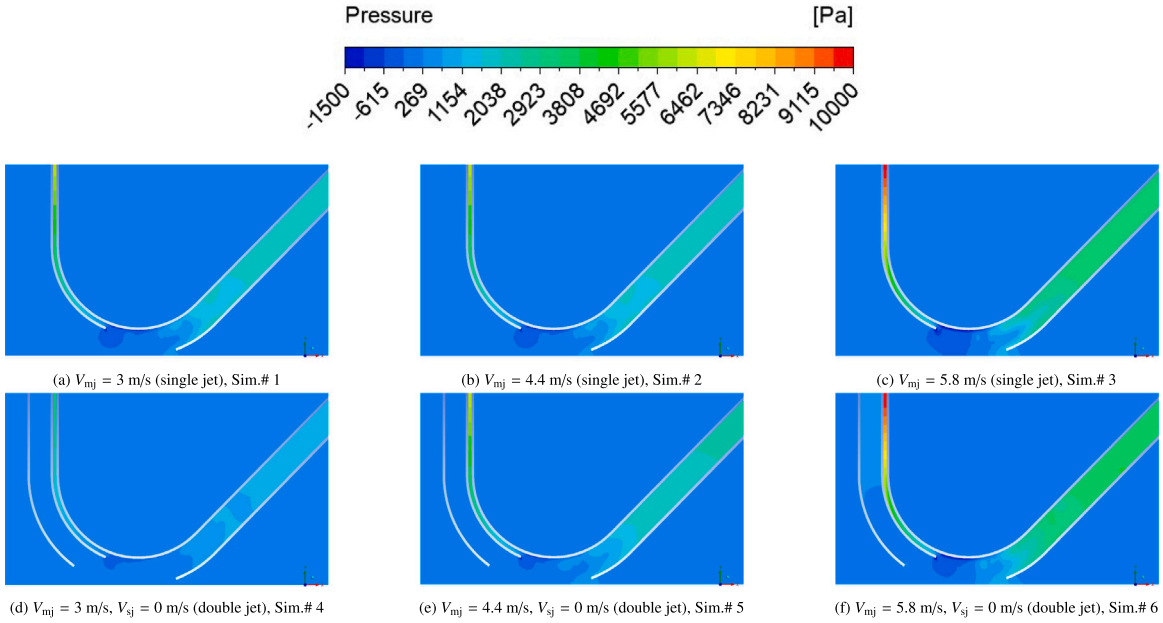

(a) V_{mj} = 3 m/s (single jet), Sim.# 1 (b) V_{mj} = 4.4 m/s (single jet), Sim.# 2 (c) V_{mj} = 5.8 m/s (single jet), Sim.# 3

(d) V_{mj} = 3 m/s, V_{sj} = 0 m/s (double jet), Sim.# 4 (e) V_{mj} = 4.4 m/s, V_{sj} = 0 m/s (double jet), Sim.# 5 (f) V_{mj} = 5.8 m/s, V_{sj} = 0 m/s (double jet), Sim.# 6

Fig. 9. Effect of main jet velocity (V_{mj}) on static pressure contours for single and double-jet configurations. In the single-jet cases, strong pressure gradients form between the collector's upper surface and the rigid bed, enhancing ambient water entrainment with increasing V_{mj}. The double-jet configuration shows a similar trend but with weaker pressure gradients, leading to reduced suction and entrainment.

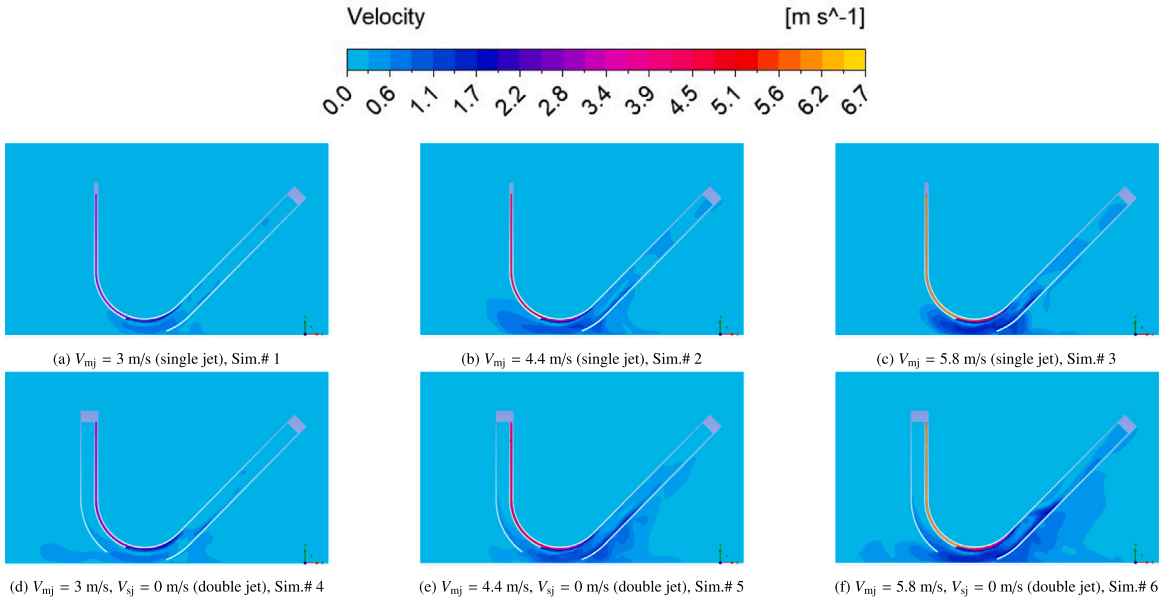

(a) V_{mj} = 3 m/s (single jet), Sim.# 1 (b) V_{mj} = 4.4 m/s (single jet), Sim.# 2 (c) V_{mj} = 5.8 m/s (single jet), Sim.# 3

(d) V_{mj} = 3 m/s, V_{sj} = 0 m/s (double jet), Sim.# 4 (e) V_{mj} = 4.4 m/s, V_{sj} = 0 m/s (double jet), Sim.# 5 (f) V_{mj} = 5.8 m/s, V_{sj} = 0 m/s (double jet), Sim.# 6

Fig. 10. Effect of main jet velocity (V_{mj}) on velocity contours for single and double-jet configurations. In both the collector, higher (V_{mj}) improves flow adherence to the upper curved plate, enhances suction, and increases collection duct flow rate (Q_c) through stronger entrainment. However, lower (V_{mj}) in the double-jet collector causes lateral sideways spillage, reducing Q_c.

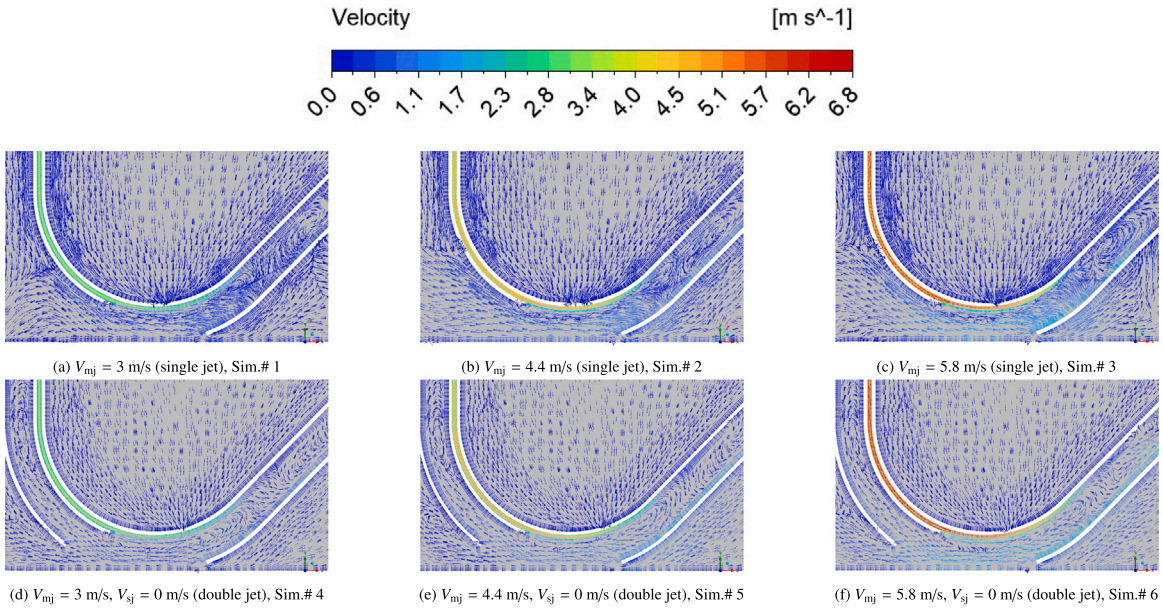

Fig. 11. Effect of main jet velocity (V_{mj}) on velocity vector under single and double-jet configurations. The overall flow pattern remains similar; increasing V_{mj} enhances velocity magnitudes upstream, downstream, and within the collection duct. The double-jet collector shows lower velocities due to the zero velocity in the secondary jet duct, which recirculates part of the flow back into the secondary duct.

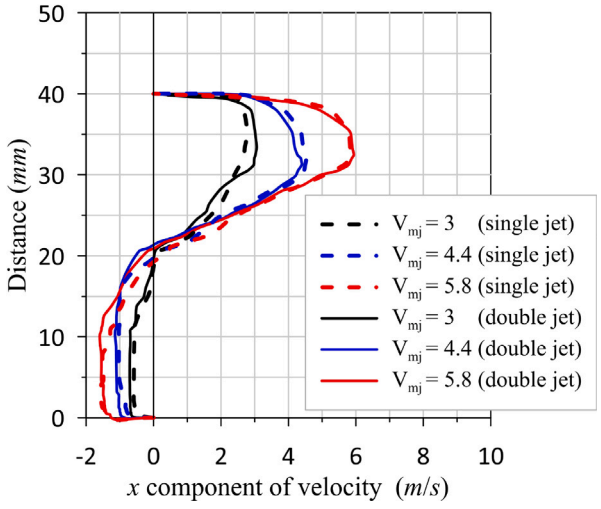

Fig. 12. Time-averaged velocity profiles beneath the collector for single-jet (dashed) and double-jet (solid) configurations. X-component of velocities are small and negative near the bed due to recirculation, increase sharply with height, and slightly decrease near the collector upper plate. Higher V_{mj} leads to larger velocity magnitudes, broader profiles, and stronger recirculation, with double-jet cases consistently producing higher velocities.

Fig. 15 presents the velocity contours for varying secondary jet velocities (V_{sj}) in a double-jet configuration (Figs. 15(a)–15(c)). It can be seen that the introduction of a secondary jet significantly alters the velocity field and increases the velocity magnitude underneath the collector, resulting in higher volumetric flow rates inside the collection duct Q_c, upstream spillage Q_{us}, and downstream spillage Q_{ds}. This is mainly due to the interaction of the main jet flow with the secondary jet flow. At the same time, the secondary jet partly suppresses backflow beneath the collector by weakening recirculating vortices and maintaining flow attachment.

Fig. 16 presents a close-up of the velocity vector fields for varying secondary jet velocities (V_{sj}) in double-jet configurations. When V_{sj} is 0 m/s (Fig. 16(a)) and 0.48 m/s (Fig. 16(b)), a noticeable recirculation zone forms underneath the collector. This occurs because the jet momentum is not strong enough to direct the incoming flow fully into the collection duct, allowing reverse flow and vortices to develop below the collector. However, when the secondary jet velocity is increased to 0.96 m/s (Fig. 16(c)), this recirculation zone disappears. The stronger jet provides sufficient momentum to overcome flow separation and guides most of the water directly into the collection duct. As a result, the flow beneath the collector becomes streamlined, leading to higher Q_c in collection for secondary jet velocity of 0.96 m/s (Table 1, Sim. # 8). These observations are further supported by the streamline plots presented in Fig. 35 in the Appendix.

Fig. 17 presents the time-averaged velocity profiles underneath the collector for different secondary jet velocities in the double-jet configuration. When $V_{sj} = 0$, a strong recirculation zone develops near the bed, resulting in negative velocities in the x - direction close to the seabed. Introducing the secondary jet alters the flow field pattern: at V_{sj} = 0.48 m/s, the flow reversal weakens but still exhibits a negative x-velocity component near the bed. At the higher velocity (V_{sj} = 0.96 m/s), the near-bed flow direction shifts to a positive x-velocity component, which helps to suppress strong flow reversal and recirculation close to the seabed. In the upper region of the velocity profile, all cases converge to similar values, suggesting that the influence of the secondary jet is mainly limited to the near-bed region. It is also observed that at lower secondary jet velocities ($V_{sj} = 0$ and 0.48 m/s), negative velocities occur near the bed due to strong recirculation zones generated beneath the collector.

Fig. 18 presents the effect of Q_{sj} on the flow rates in and around the collector head. The increase in Q_{sj} causes a linear increase in the Q_c values, which is mainly due to the presence of a stronger secondary jet that develops a larger pressure drop underneath the collector and pushes more water into the collection duct. However, a significant decrease can be observed in Q_{us}, while Q_{ds} values remain almost constant with respect to Q_{sj}. The sideways spillage increases with an increase in Q_{sj}, which leads to an increase in net water entrainment. This means that the secondary jet helps to draw more water into the collection duct. However, it causes more sideways spillage.

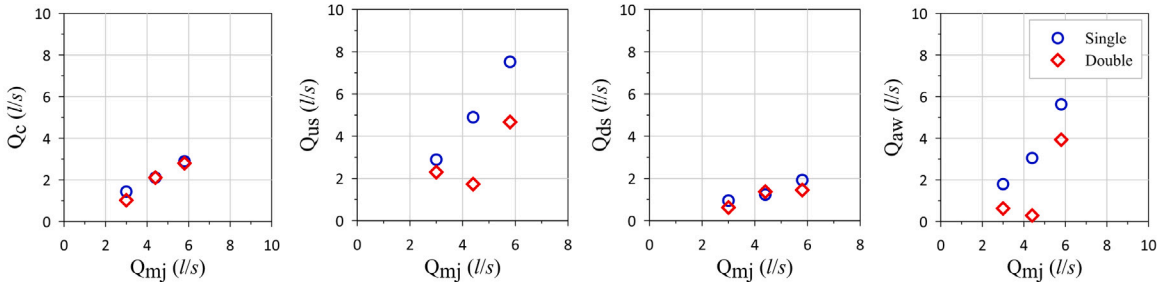

(a) Variation of Q_c with respect to Q_{mj} (b) Variation of Q_{us} with respect to Q_{mj} (c) Variation of Q_{ds} with respect to Q_{mj} (d) Variation of Q_{aw} with respect to Q_{mj}

Fig. 13. Effect of Q_{mj} on the flow rates in and around the collector head for single and double-jet collector. Increasing Q_{mj} enhances the *Coandă effect*, leading to higher Q_c, Q_{us}, and Q_{ds}, with the double-jet collector showing slightly lower Q_c due to backflow into the inactive secondary slot. The sideways flows (Q_{ss}) contribute to the system, except for noticeable spillage at Q_{mj} = 5.8 m/s in the double-jet configuration. The net ambient water entrainment (Q_{aw}) also becomes larger with an increase in Q_{mj} in the single-jet collector.

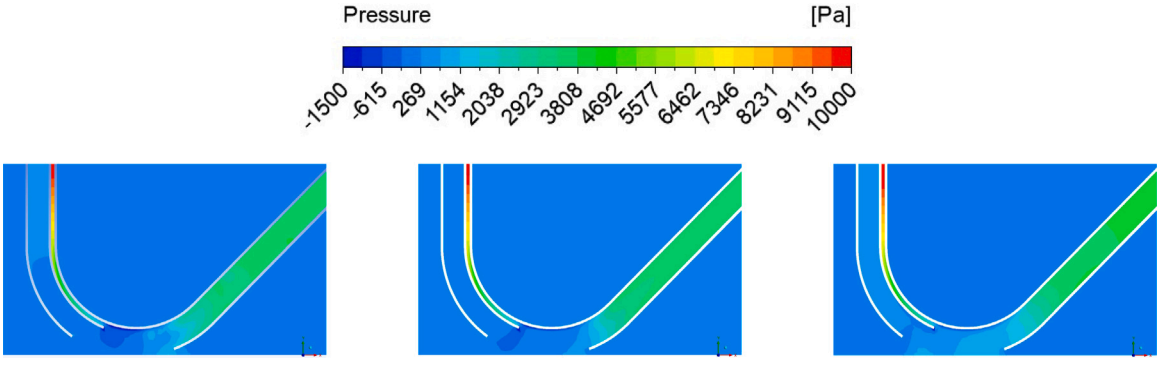

(a) V_{sj} = 0 m/s, Sim. # 6 (b) V_{sj} = 0.48 m/s, Sim. # 7 (c) V_{sj} = 0.96 m/s, Sim. # 8

Fig. 14. Static pressure contours for varying secondary jet velocities (V_{sj}) in the double-jet configuration. The increase in V_{sj} leads to a decrease in maximum pressure drop compared to the zero-velocity case, thereby reducing the net ambient water entrainment.

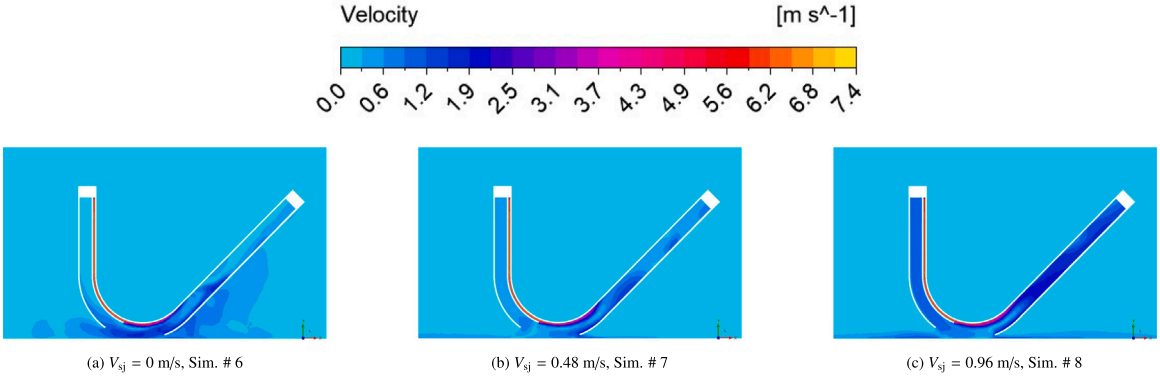

(a) V_{sj} = 0 m/s, Sim. # 6 (b) V_{sj} = 0.48 m/s, Sim. # 7 (c) V_{sj} = 0.96 m/s, Sim. # 8

Fig. 15. Velocity contours for varying secondary jet velocities (V_{sj}) in the double-jet configuration. Increasing V_{sj} strengthens the velocity field beneath the collector, resulting in higher Q_c, Q_{us}, and Q_{ds}. The interaction of the main and secondary jets reduces ambient water entrainment and spillage while suppressing backflow by weakening recirculation zones and maintaining flow attachment.

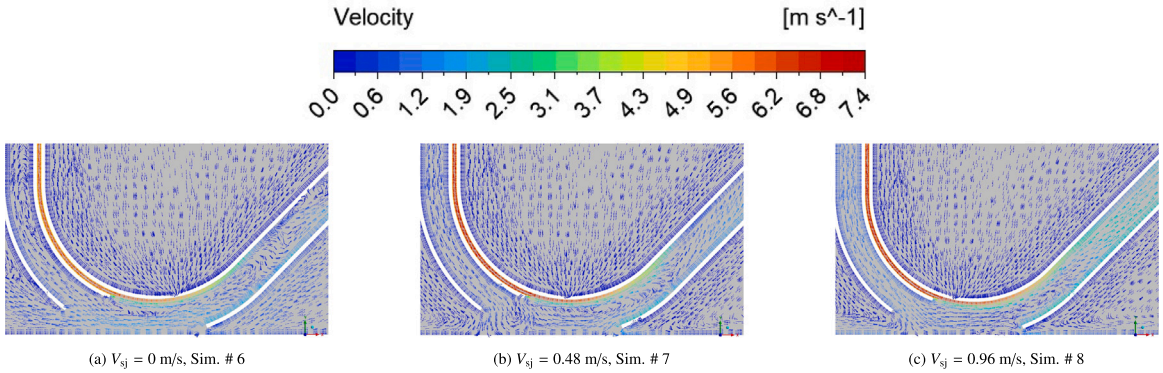

(a) V_{sj} = 0 m/s, Sim. # 6 (b) V_{sj} = 0.48 m/s, Sim. # 7 (c) V_{sj} = 0.96 m/s, Sim. # 8

Fig. 16. Velocity vector fields for varying secondary jet velocities (V_{sj}) in the double-jet configuration. At low V_{sj} (0 – 0.48 m/s), the recirculation zone forms beneath the collector due to insufficient jet momentum, allowing reverse flow and vortices to develop. Increasing V_{sj} to 0.96 m/s eliminates this recirculation, streamlines the flow into the collection duct, and increases Q_c.

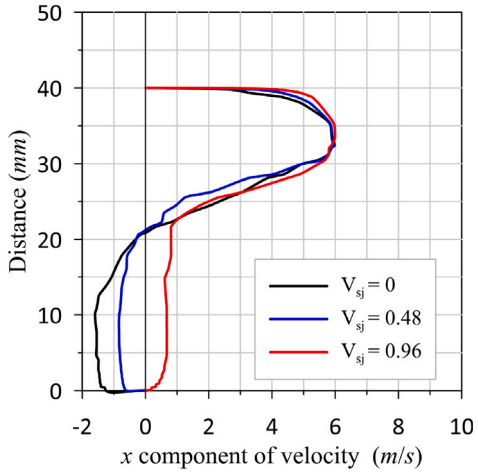

Fig. 17. Time-averaged x-component of velocity underneath the collector for different secondary jet velocities (V_{sj} = 0, 0.48, and 0.96 m/s). Increasing V_{sj} modifies the velocity distribution by reducing near-bed velocities, thereby suppressing recirculation, while enhancing momentum transfer in the mid-region. At higher V_{sj}, the profiles converge in the upper region, indicating that the influence of the secondary jet is mainly confined to the near-bed and mid-depth regions.

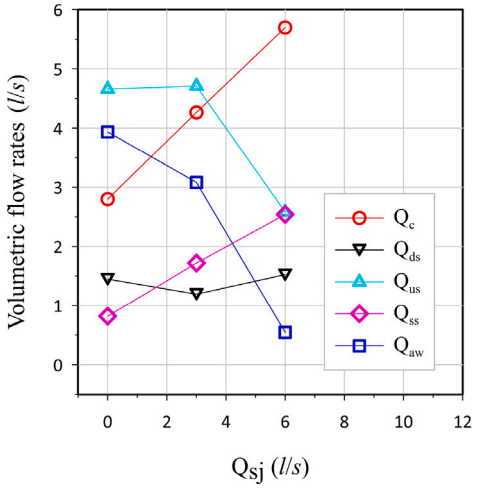

Fig. 18. Effect of Q_{sj} on the flow rates in and around the collector head. Increasing Q_{sj} produces a nearly linear rise in Q_c, due to larger maximum pressure drop beneath the collector, while Q_{us} shows a significant decrease with larger values of Q_{sj}. A higher Q_{sj} also causes more sideways spillage (Q_{ss}). However, a decrease in net water entrainment Q_{aw} is observed with increase in Q_{sj}.

3.3. Effect of radius of curvature (R)

The radius of curvature R was systematically varied to 100, 125, and 150 mm. The main jet velocity (V_{mj}), secondary jet velocity (V_{sj}), and bottom clearance were kept constant at 5.8 m/s, 0.96 m/s, and 7.5 mm, respectively.

Fig. 19 presents the pressure contours for varying radius of curvature (R) in the double-jet configuration. It can be observed that the pressure gradient becomes smaller underneath the collector as the radius of curvature (R) increases (Figs. 19(a)–19(c)). This leads to a weaker flow attachment along the curved surface, which leads to reduced suction and lesser net ambient water entrainment (Fig. 19(a)). These observations are further supported by the variation of the pressure drop just under the collector's plate for double-jet configurations, shown in Fig. 32 in Appendix.

Fig. 20 presents the velocity contours for varying radius of curvature (R) in the double-jet configuration. As the radius of curvature increases, the high-velocity jet remains more closely attached to the curved surface of the upper plate due to a stronger *Coandă effect*. This promotes a more directed and smoother movement of flow towards the collection duct (Fig. 20(c)). However, at smaller values of R equal to 100 mm (Fig. 20(a)) and 125 mm (Fig. 20(b)), the jet detaches earlier from the curved surface, leading to a broader spreading of the jet and the formation of a recirculation zone underneath the collector, which results in higher sideways spillage of the collector. Similarly, the velocity vector diagrams (Fig. 21) show the adherence and recirculation zones underneath the collector. A large recirculation zone extended up to the collection duct entrance can be observed for R equal 100 mm (Fig. 21(a)). However, for larger values of R, the recirculation zone underneath the collector is partially suppressed (Fig. 21(c)). These findings are further confirmed by streamline plots presented in Fig. 36 of Appendix.

Fig. 22 shows the time-averaged x-component of velocity underneath the collector for different radii of curvature (R = 100, 125, and 150 mm). For the smaller radius (R = 100 mm and R = 125), the x-component of velocity shows negative values near the bed, indicating stronger recirculation of flow (R = 100). However, as the radius of curvature increases to 150 mm, the near-bed velocity becomes positive and smoother, meaning reduced recirculation and more stable flow conditions.

Fig. 23 presents the effect of the radius of curvature of the upper plate of the collector on the flow rates in and around the collector

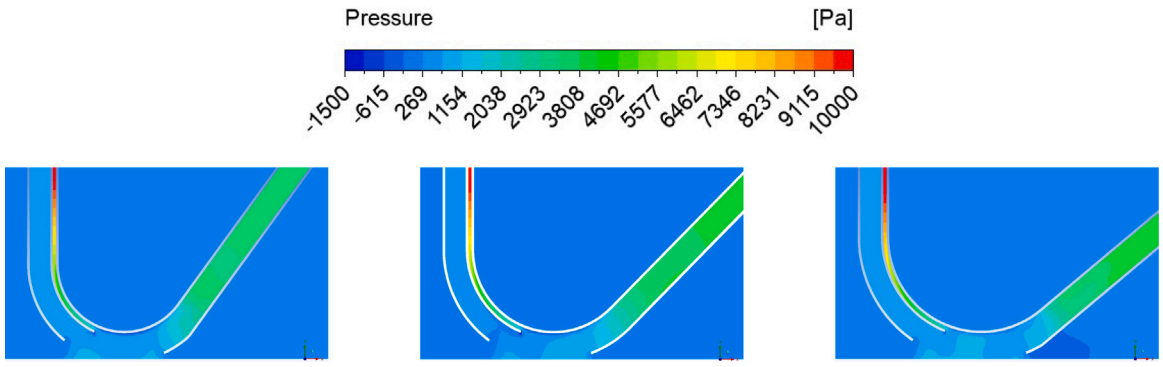

(a) R = 100 mm, Sim.# 9 (b) R = 125 mm, Sim.# 8 (c) R = 150 mm, Sim.# 10

Fig. 19. Static pressure contours for varying radius of curvature (R) in the double-jet configuration. Increasing R strengthens the *Coandă* attachment of the jet along the upper plate, producing a more distinct under-pressure region beneath the collector. This enhances suction and ambient water entrainment, with the largest effect observed at R = 150 mm.

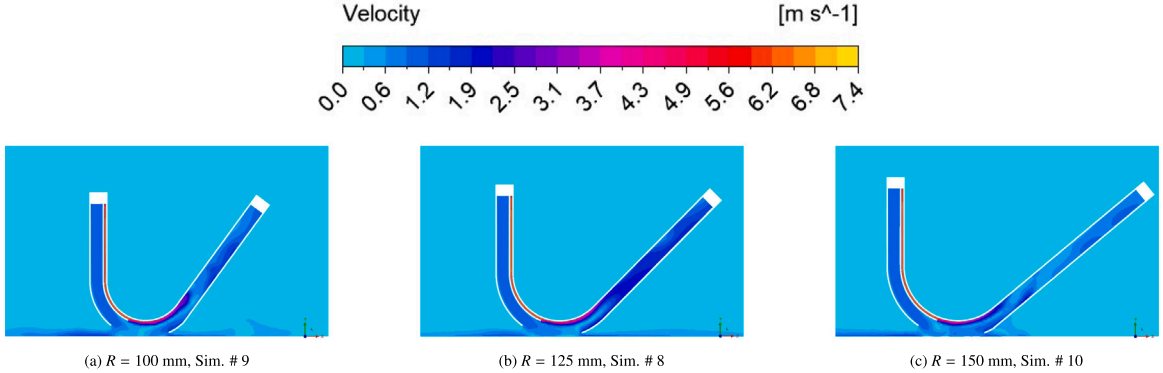

(a) R = 100 mm, Sim. # 9 (b) R = 125 mm, Sim. # 8 (c) R = 150 mm, Sim. # 10

Fig. 20. Velocity contours for varying radius of curvature (R) of the upper plate in the double-jet configuration. Larger R values strengthen the *Coandă effect*, keeping the jet attached to the curved surface and directing flow smoothly into the collection duct. At smaller R (100–125 mm), early jet detachment causes broader spreading and recirculation beneath the collector, leading to increased sideways spillage.

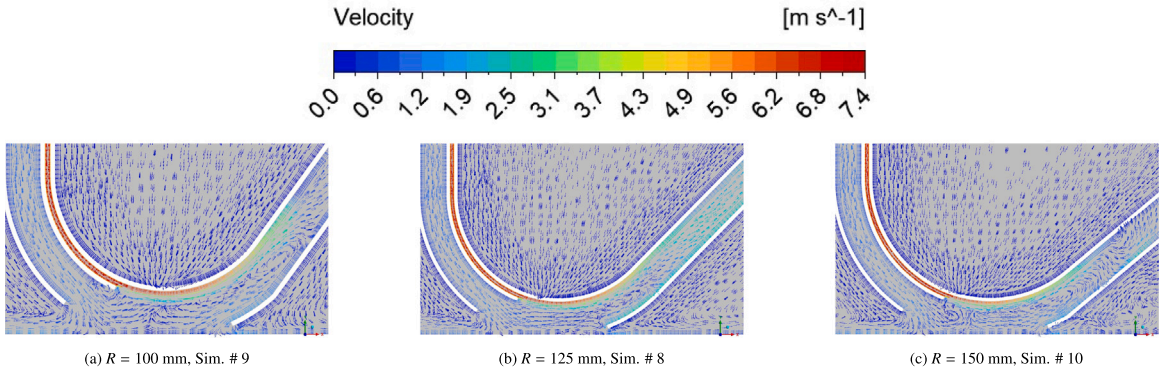

(a) R = 100 mm, Sim. # 9 (b) R = 125 mm, Sim. # 8 (c) R = 150 mm, Sim. # 10

Fig. 21. Velocity vector fields for varying radius of curvature (R) in the double-jet configuration. Increasing R improves *Coandă* attachment, keeping the jet aligned with the curved surface and smoothly directing flow into the collection duct. At a smaller R = 100 mm, early jet detachment induces strong recirculation and lateral spreading beneath the collector.

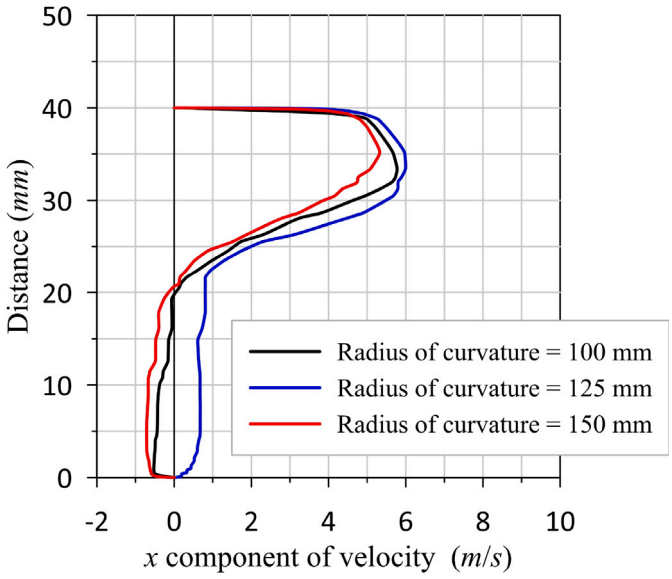

Fig. 22. Time-averaged x-component of velocity underneath the collector for different radius of curvature (R = 100, 125, and 150 mm). Increasing the radius of curvature reduces near-bed velocities and recirculation while promoting smoother momentum transfer in the mid-region. All profiles converge in the upper region, indicating that the effect is mainly confined to the near-bed and mid-depth zones.

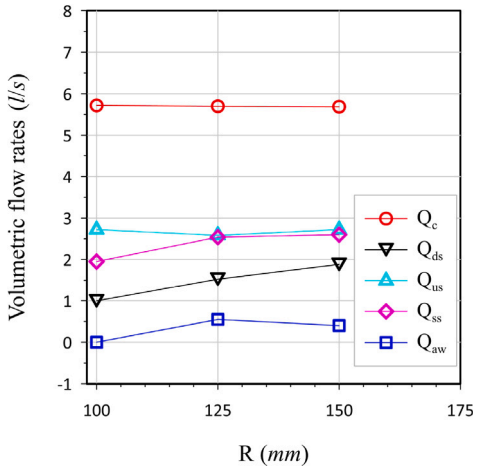

Fig. 23. Effect of radius of curvature (R) of the collector's upper plate on the flow rates in and around the collector head. The flow rate Q_c and Q_{us} in the collection duct remains nearly constant for all values of R. Downstream spillage (Q_{ds}) increases with R. A gradual increase in sideways spillage is also observed with larger R, as the jet diffuses more widely along the curved surface and a greater portion of the entrained flow escapes laterally rather than entering the collection duct. Therefore, a mild net ambient water entrainment is observed with an increase in radius of curvature R.

head. The volumetric flow rate Q_c is almost constant for each radius of curvature (R). As the radius of curvature R increases, the upstream spillage Q_{us} remains nearly constant up to 125 mm but shows a slight decrease at 125 mm, likely due to stronger flow recirculation causing more upstream flow reversal. The downstream spillage Q_{ds}, increases with R. Further, the radius of curvature does not significantly influence Q_{aw}, since the sideways spillage is larger under the applied jet velocity conditions. Further, a gentle increase in sideways spillage can be observed with an increase in R, similar to results observed in Jia et al. (2024).

3.4. Effect of bottom clearance (C)

The bottom clearance (C) was systematically varied to 7.5, 13, and 18 mm, while the main jet velocity (V_{mj}) and secondary jet velocity (V_{sj}) were kept constant at 5.8 m/s and 0.96 m/s, respectively. The radius of curvature (R) was also kept constant at 125 mm.

Fig. 24 presents the static pressure contours for varying bottom clearance (C) in double-jet configuration. At a smaller bottom clearance of 7.5 mm (Fig. 24(a)) and 13 mm (Fig. 24(b)), a relatively smaller under-pressure zone develops beneath the collector. In contrast, at a larger bottom clearance of 18 mm (Fig. 24(c)), a wider and larger under-pressure region is observed. As shown in the pressure-drop diagram along the y-axis underneath the collector, from bed to upper plate of the collector (Fig. 33), a smaller bottom clearance produces a smaller pressure drop, signifying a weaker suction effect.

Fig. 25 shows the velocity contours for different bottom clearances (C) in the double-jet configuration. At the smallest clearance of 7.5 mm, the jet velocity near the curved plate is relatively weak, resulting in lower suction beneath the collector and limited entrainment of ambient water. When the clearance is increased to 13 mm, the velocity core strengthens, leading to greater suction and enhanced inflow of ambient water. At the largest clearance of 18 mm, the velocity distribution further intensifies, allowing maximum net ambient water entrainment (Fig. 25(c)). Similarly, the close-up of the velocity vectors (Fig. 26 shows the recirculation zones and flow reversal beneath the collector for varying bottom clearance. The larger recirculation zone is evident in the case of bottom clearance equal to 7.5 mm (Fig. 26(a)). However, as the bottom clearance C increases to 13 mm (Fig. 26(b)) and 18 mm (Fig. 26(c)), a noticeable recirculation zone forms just outside the secondary jet opening. This recirculating flow helps guide more surrounding water towards the suction region of the collector. These findings are further confirmed by the streamline plots presented in Fig. 37 in Appendix.

In Fig. 27, time-averaged velocity profiles beneath the collector are shown for varying bottom clearances (C). For the smallest clearance of 7.5 mm, the x-component of velocity remains positive near the bed, primarily due to better flow adherence to the Tabled plate and the formation of a stable flow beneath the collector. As the bottom clearance (C) increases to 13 and 18 mm, the larger gap allows more space for flow development and entrainment, as well as stronger jet acceleration along the bed. This results in flow recirculation beneath the collector, producing negative velocities near the bed before recovering to positive values and reaching a peak velocity.

Fig. 28 presents the effect of bottom clearance on the flow rates in and around the collector head. It can be observed that the flow rate in the collection duct Q_c remains constant across different bottom clearance (C) values. The increase in bottom clearance leads to a rapid decrease in upstream spillage Q_{us}, which is due to smaller backflow and larger opening to the flow upstream of the collector. Further, a gentle increase in the downstream spillage Q_{ds} is observed with an increase in bottom clearance. Further, it can be seen that the increase in bottom clearance (C) significantly enhances the ambient water entrainment Q_{aw} due to the larger volumetric space available for water to be drawn in from underneath the collector, which is consistent with the findings of Alhaddad et al. (2024).

3.5. Effect of froude number Fr

The Froude number (Fr) plays an important role in governing the hydrodynamic behavior of jet-induced flows. Since the collector has two water jets, the Froude number used here is defined as:

$$Fr = \frac{U}{\sqrt{gh}} \tag{2}$$

where U is the layer-average velocity at the center beneath the collector, g is the acceleration due to gravity, and h is the vertical distance from the rigid bed to the upper plate of the collector.

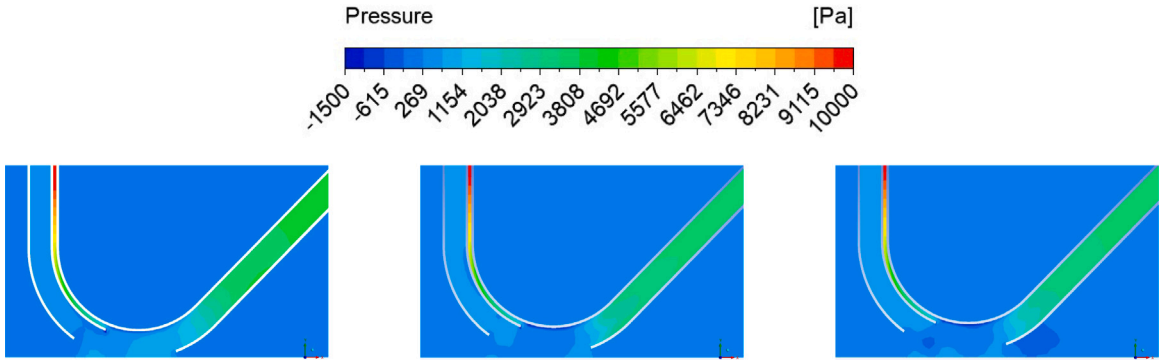

(a) C = 7.5 mm, Sim.# 8 (b) C = 13 mm, Sim.# 11 (c) C = 18 mm, Sim.# 12

Fig. 24. Pressure contours for varying bottom clearance (C) in the double-jet configuration. At smaller clearances (7.5 mm and 13 mm), a relatively small and lower-pressure zone forms beneath the collector. Increasing the clearance to 18 mm produces a broader and larger under-pressure region, which increases ambient water entrainment.

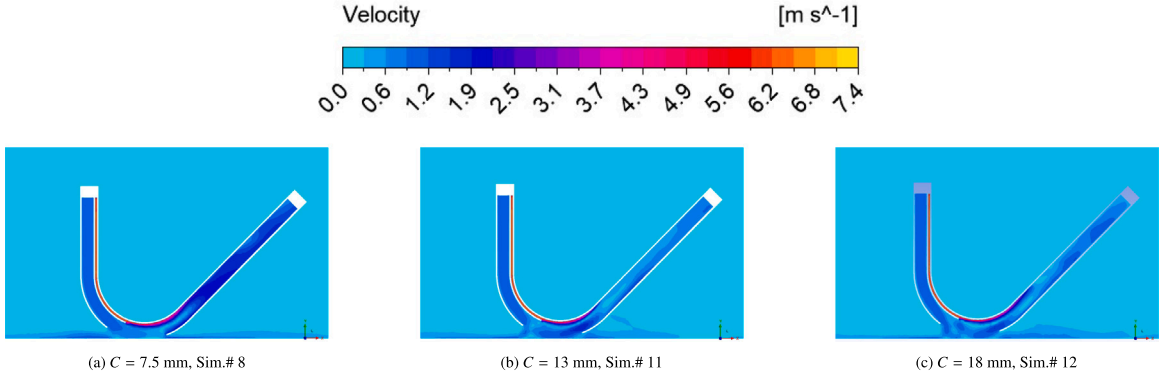

(a) C = 7.5 mm, Sim.# 8 (b) C = 13 mm, Sim.# 11 (c) C = 18 mm, Sim.# 12

Fig. 25. Velocity contours for varying bottom clearance (C) in the double-jet configuration. At smaller clearance, the jet velocity is weaker, resulting in lower suction and limited entrainment. Increasing clearance strengthens the velocity core, enhances suction, and allows greater ambient-water entrainment.

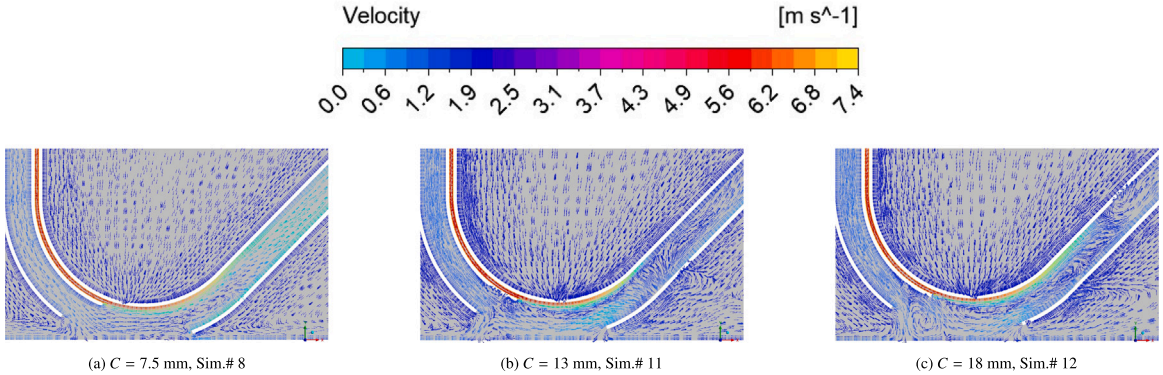

(a) C = 7.5 mm, Sim.# 8 (b) C = 13 mm, Sim.# 11 (c) C = 18 mm, Sim.# 12

Fig. 26. Velocity vector fields for varying bottom clearance (C) in the double-jet configuration. At a small clearance of 7.5 mm, strong downward jets interact with the rigid bed, producing pronounced recirculation zones and flow reversal beneath the collector, causing sideways deflection and less efficient suction. Increasing C to 13 mm and 18 mm reduces jet-bed interaction, resulting in smoother and more streamlined flow paths. At 18 mm, a recirculation zone forms just outside the secondary jet opening, guiding more surrounding water towards the suction region and enhancing ambient water entrainment.

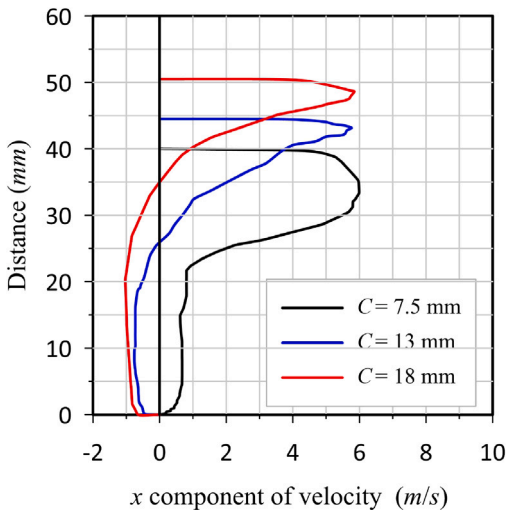

Fig. 27. Time-averaged x-component of velocity beneath the collector for different bottom clearances (C = 7.5, 13, and 18 mm). A smaller clearance promotes stable flow with positive near-bed velocity, while larger clearances allow greater flow entrainment and jet acceleration, leading to recirculation and negative velocities near the bed before attaining similar peak values.

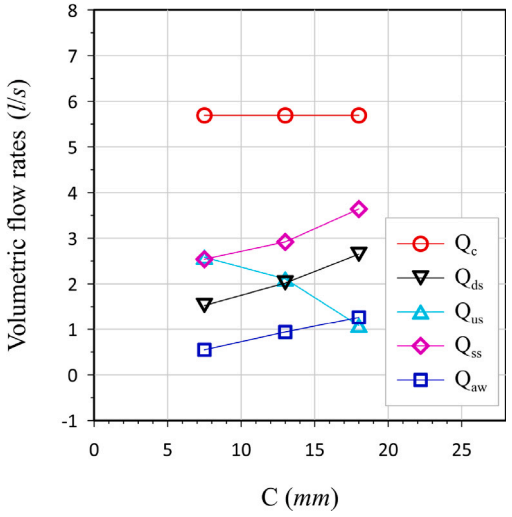

Fig. 28. Effect of bottom clearance (C) on the flow rates in and around the collector head for a double-jet collector. The flow rate Q_c in the collection duct remains nearly constant for all bottom clearances. Increasing the C leads to smaller upstream spillage Q_{us}, and a gradual increase in downstream spillage (Q_{ds}). At the same time, sideways spillage (Q_{ss}) also gradually increases with increased C. However, a rapid change in the (Q_{aw}) is observed due to the larger space beneath the collector.

Fig. 29 presents the effect of Froude number Fr on the flow rates in and around the collector head. It can be observed that increasing Q_{mj} leads to higher Froude number Fr in both configurations due to the increased flow velocities under the collector (Alhaddad et al., 2023). The results show that the upstream spillage (Q_{us}) is higher in the single-jet configuration than in the double-jet case. This occurs because the presence of two jet ducts generates stronger suction beneath the collector. Furthermore, in the case of a single jet, larger backflow is observed, creating a stronger recirculation zone underneath the collector and leading to larger upstream spillage. A milder rise in the Q_{ds} values is observed with an increase in Fr for both the configurations. This suggests that the majority of entrained flow follows the collector surface, limiting the downward spillage Q_{ds}; a higher Fr amplifies the *Coandă effect*. In the single-jet configuration, the Q_{ss} are observed to be smaller for all Fr values, since almost all of the entrained flow is directed into the collector. However, the double-jet configuration exhibits a mild increase in Q_{ss} with an increase in Fr, indicating that part of the entrained water is diverted laterally due to recirculation induced by the secondary duct. Therefore, a larger Q_{aw} can be observed in the case of single-jet collectors compared to double-jet collectors for all values of Fr.

4. Conclusions

This study investigated the flow behavior in a *Coandă effect*-based collector under different operational and geometric parameters. The results show that the main jet adheres to the curved upper plate due to the *Coandă effect*, generating an under-pressure zone that entrains ambient water into the collection duct. As the jet moves along the surface, flow separation from the curved upper plate and flow recirculation may occur, leading to upstream, downstream and sideways spillage. In a single-jet collector, the increase in main jet velocity enhances the flow attachment and the developed pressure gradient, resulting in higher ambient water entrainment.

In the case of a double-jet collector, when a secondary jet duct is present but inactive (i.e., zero velocity), the backflow diverts ambient water towards the inactive jet duct, causing more spillage, particularly at lower main jet velocities (3 m/s). At higher main jet velocities (4.4 – 5.8 m/s), even with the secondary jet inactive, larger pressure differences develop, allowing greater ambient water entrainment. This increases the flow rate in the collection duct and also promotes the spillage upstream, downstream and sideways. Further, the introduction of a secondary jet to the collector enhances suction and helps to maintain flow adherence to the curved surface, increasing the collection duct flow rate (Q_c). However, higher secondary jet velocities also promote significant sideways spillage.

The increase in radius of curvature (100 - 150 mm) of the collector has minimal effect on the volumetric flow rate in the collection duct Q_c. However, at a higher radius of curvature (R = 150 mm), the smoother upper plate profile leads to lesser sideways spillage. Similarly, an increase in the bottom clearance (7.5 - 18 mm) does not affect the flow rate inside the collection duct. The increase in bottom clearance increases the net ambient water entrainment. However, at a larger bottom clearance, more surrounding water enters beneath the collector. As the collection duct is unable to carry flow beyond its capacity, this excess flow results in increased spillage around the collector.

Finally, the effect of the Froude number (Fr) on the flow behavior around the collector is also investigated. It is observed that an increase in Fr enhances the *Coandă effect*, drawing more surrounding water into the system and resulting in a higher flow rate in the collection duct. In the single-jet collector, ambient water entrainment is higher compared to the double-jet collector, primarily due to the larger upstream flow area available for inflow and the reduced upstream outflow from the collector.

5. Limitations and future scope

In this section, selected limitations of the present study are discussed to help identify directions for future research.

The numerical simulations in this study employ a Reynolds-averaged Navier–Stokes (RANS) formulation with the k–ω SST turbulence model. While this approach is computationally efficient and widely used, it limits the ability to fully resolve fine-scale boundary-layer structures, particularly in regions of strong shear (Menter, 1994; Wilcox et al., 1998). As a result, predictions of near-wall velocities, turbulence-induced mixing, and jet attachment may be affected, all of which are critical for accurately estimating water entrainment and sediment transport. Higher-fidelity turbulence modeling approaches, such as

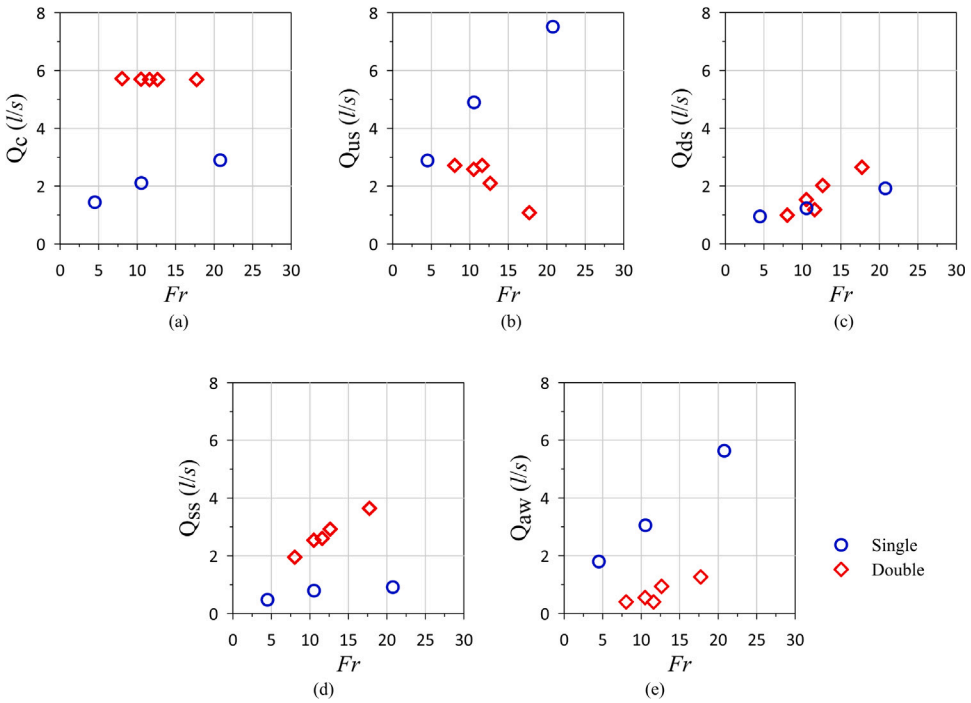

Fig. 29. Effect of Froude number (F_r) on the flow rates in and around the collector head for single and double-jet collector. The increase in Fr leads to larger Q_c and Q_{us}, with upstream spillage being higher in the single-jet configuration due to smaller recirculation of flow. The downstream spillage (Q_{ds}) shows a mild increase as most flow stays attached to the collector. The sideways spillage also increases with the rise in Fr, that results in rapid increase in ambient water entrainment (Q_{aw}) in single-jet configuration.

large-eddy simulation (LES) or hybrid RANS–LES methods, could provide improved resolution of near-wall and recirculation dynamics and represent an important direction for future work.

In addition, the seabed is represented as a rigid bed with a no-slip boundary condition to simplify the numerical setup and enable comparison with previous experimental studies. Although this assumption captures the primary flow features and ambient-water entrainment around the Coandă-effect-based collector, it does not fully reflect realistic deep-sea conditions, where the seabed may deform or erode. Bed deformation or erosion could alter near-bed velocities, modify recirculation zones, and increase sediment suspension. Moreover, sediment-laden flow may influence turbulence characteristics, jet attachment, and entrainment efficiency. In the present simulations, no two-way coupling between sediment transport and the flow is considered. These effects could change the relative amounts of water entering the collection duct versus spilling around the collector. Future studies incorporating deformable or erodible seabeds and coupled sediment-transport models are therefore required to improve predictive capability and better assess environmental impacts.

With respect to the generation of deep-sea sediment plumes, it should be noted that this process cannot be explained solely by the amount of entrained water. As reported by Alhaddad et al. (2024), two primary sources contribute to plume formation: (i) the sediment–water mixture discharged at the rear of the collector through the discharge duct, and (ii) sediment–water spillage behind the collector head. Both sources generate turbidity currents that eventually interact downstream of the collector. In this context, water entrainment plays an important role by contributing to the flow rate through the collection duct. During operation, the discharged fluid is a sediment–water mixture, and its flow rate is a key parameter in numerical models used to predict plume extent. Furthermore, increased entrained-water flow rates result in higher near-bed velocities, enhancing the erosive capacity of the flow and promoting sediment disturbance. Although sediment transport and plume development are not explicitly modeled in this study, the quantified water entrainment provides essential hydrodynamic input for future coupled sediment–plume modeling efforts.

Finally, the simulations presented in this study consider stationary collectors, whereas collectors will be in motion during real mining operations. The forward speed of the collector can significantly influence the flow dynamics around the collector, including water entrainment and near-bed flow characteristics (Alhaddad et al., 2023). Accounting for collector motion therefore represents another important direction for future modeling studies.

CRediT authorship contribution statement

Lalit Kumar: Writing – original draft, Visualization, Validation, Methodology, Investigation, Formal analysis, Data curation, Writing – review & editing. **Sebastiaan Mulders:** Writing – review & editing, Supervision, Resources, Project administration, Funding acquisition, Conceptualization, Methodology. **Said Alhaddad:** Writing – review & editing, Supervision, Resources, Project administration, Methodology, Investigation, Funding acquisition, Formal analysis, Conceptualization, Visualization.

Declaration of competing interest

The authors declare that they have no known competing financial interests or personal relationships that could have appeared to influence the work reported in this paper.

Acknowledgments

The authors would like to thank the Faculty of Mechanical Engineering (ME) at Delft University of Technology for supporting this research through the Cohesion Fund.

Appendix. Additional numerical results

The appendix presents additional numerical results that complement and extend the findings discussed in the main text. These results provide further insights into the influence of main jet velocity, secondary jet velocity, radius of curvature, and bottom clearance on the flow behavior and pressure distribution beneath the collector. The supplementary figures illustrate detailed variations in pressure drop, streamline patterns, and velocity fields, across different configurations.

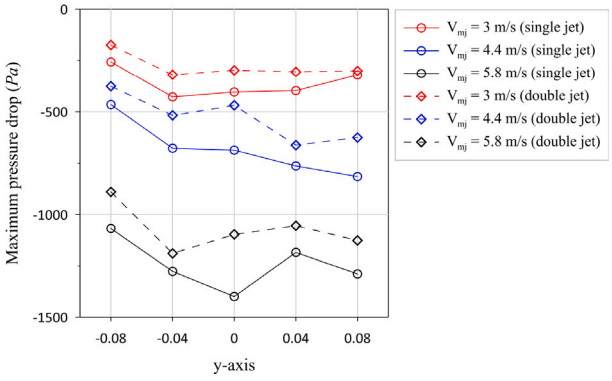

Fig. 30. Variation of pressure drop, with respect to the ambient pressure, right underneath the collector along the y-axis for different V_{mj} in both single-jet and double-jet configurations. For all cases, an increase in V_{mj} results in a higher pressure drop, indicating stronger suction beneath the collector. The double-jet configuration consistently produces a smaller pressure drop compared to the single-jet case at the same jet velocity, reflecting reduced suction and weaker ambient water entrainment.

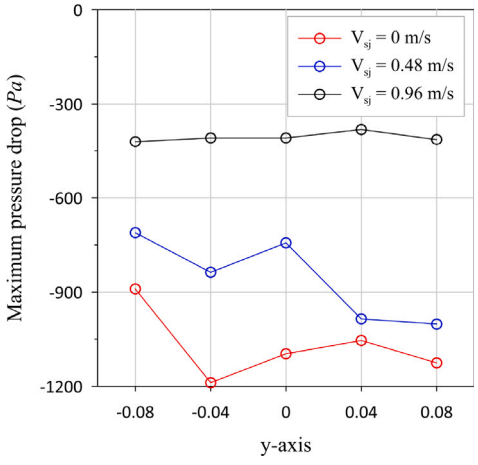

Fig. 31. Variation of maximum pressure drop underneath the collector along the y-axis for different V_{sj} in double-jet configurations. The increase in V_{sj} results in a lower pressure drop, indicating lesser suction and weaker ambient water entrainment beneath the collector.

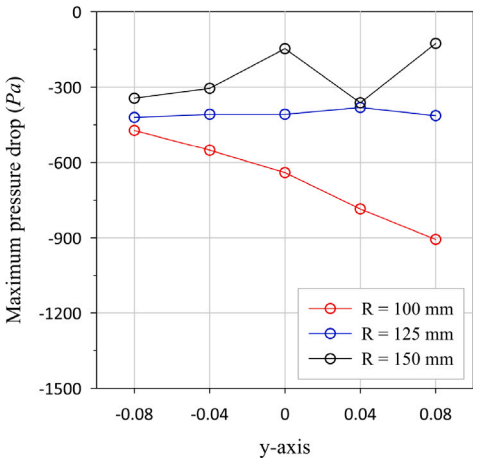

Fig. 32. Variation of pressure drop, with respect to the ambient pressure, right underneath the collector along the y-axis for different radius of curvature R of the collector. A smaller radius of curvature (R = 100 mm) produces a stronger suction beneath the collector due to enhanced jet attachment. With increasing radius of curvature of collector, the pressure drop reduces and becomes more uniform, indicating weaker suction and reduced net ambient water entrainment beneath the collector.

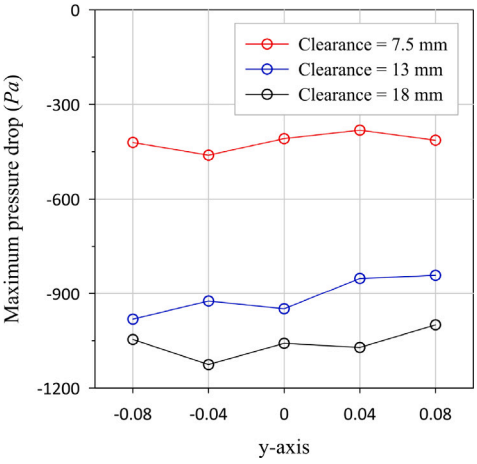

Fig. 33. Variation of pressure drop, with respect to the ambient pressure, right underneath the collector along the y-axis for different bottom clearances (7.5 mm, 13 mm, and 18 mm). The results indicate that smaller clearances (7.5 mm) produce a lower pressure difference, reflecting smaller suction beneath the collector. Increasing the clearance increases the pressure gradient, leading to a larger suction effect but larger ambient-water entrainment.

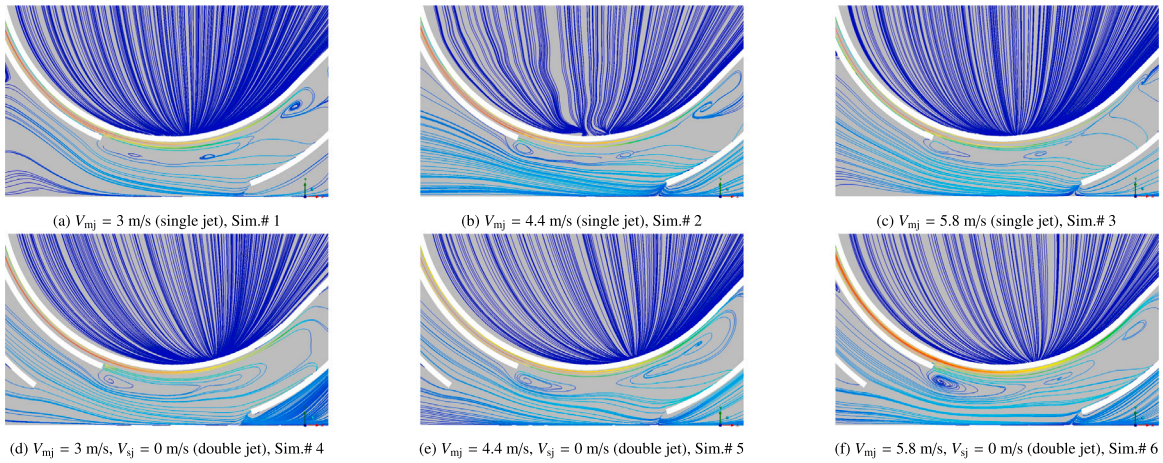

(a) V_{mj} = 3 m/s (single jet), Sim.# 1 (b) V_{mj} = 4.4 m/s (single jet), Sim.# 2 (c) V_{mj} = 5.8 m/s (single jet), Sim.# 3

(d) V_{mj} = 3 m/s, V_{sj} = 0 m/s (double jet), Sim.# 4 (e) V_{mj} = 4.4 m/s, V_{sj} = 0 m/s (double jet), Sim.# 5 (f) V_{mj} = 5.8 m/s, V_{sj} = 0 m/s (double jet), Sim.# 6

Fig. 34. Effect of main jet velocity (V_{mj}) on flow behavior under single and double-jet configurations. At higher V_{mj}, the jet forms a larger high-velocity zone, stronger turbulent mixing, and a larger recirculation region beneath the collector, enhancing ambient water entrainment and increasing Q_{us} and Q_{ds}. However, a lower V_{mj} produces a narrower jet core with weaker turbulent mixing and reduced ambient water entrainment.

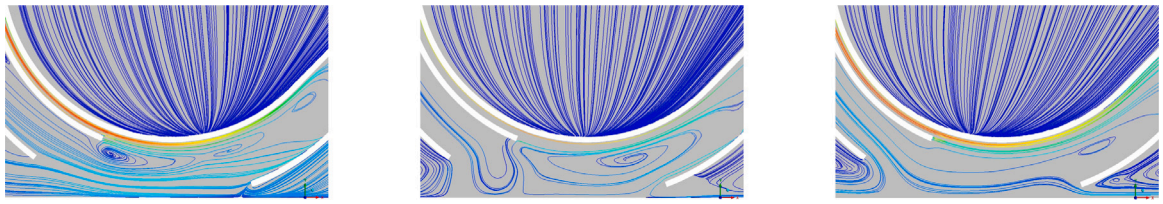

(a) V_{sj} = 0 m/s, Sim. # 6 (b) V_{sj} = 0.48 m/s, Sim. # 7 (c) V_{sj} = 0.96 m/s, Sim. # 8

Fig. 35. Streamline plots for varying secondary jet velocities (V_{sj}) in the double-jet configuration. At low V_{sj} (0–0.48 m/s), a recirculation zone develops beneath the collector, reflecting weak secondary jet influence. Increasing V_{sj} to 0.96 m/s aligns the streamlines towards the collection duct, enhancing entrainment, suppressing backflow, and increasing Q_c.

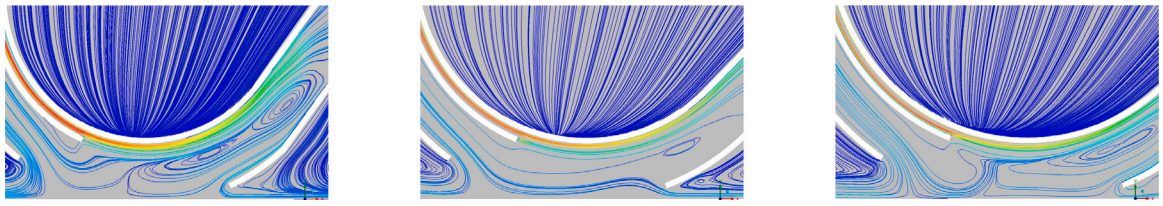

(a) R = 100 mm, Sim. # 9 (b) R = 125 mm, Sim. # 8 (c) R = 150 mm, Sim. # 10

Fig. 36. Streamline plots showing flow behavior in the double-jet configuration for varying radius of curvature (R). At smaller R = 100 mm, the jet adheres sharply to the curved surface, producing a confined trajectory, while larger R = 150 mm yields smoother attachment, stronger suction, reduced sideways spillage, and greater flow directed into the collection duct. The larger radius also generates stronger downstream wakes, which may enhance plume dispersion, although centerline velocity beneath the collector remains nearly unchanged, indicating that Q_c is largely unaffected.

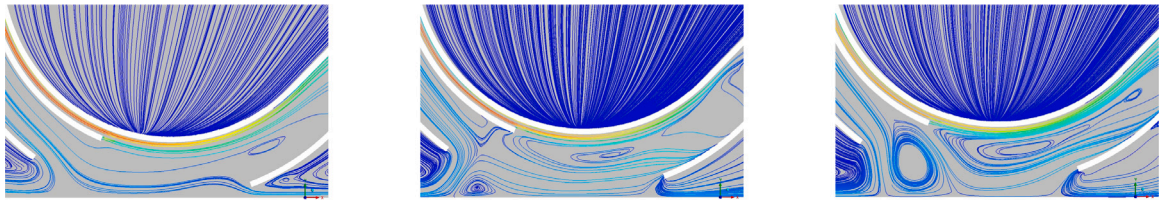

(a) C = 7.5 mm, Sim.# 8 (b) C = 13 mm, Sim.# 11 (c) c = 18 mm, Sim.# 12

Fig. 37. Streamline plots showing flow behavior in the double-jet configuration for varying bottom clearance (C). At a small clearance of 7.5 mm, the jets strongly interact with the rigid bed, creating pronounced recirculation zones, flow reversal, and sideways spillage. Higher clearance (C= 18 mm) generates additional recirculation near the secondary jet, enhancing ambient water entrainment, while stronger downstream wakes contribute to increased plume dispersion.

References

Alhaddad, S., Helmons, R., 2023. Sediment erosion generated by a Coandă-effect-based polymetallic-nodule collector. J. Mar. Sci. Eng. 11 (2), 349.

Alhaddad, S., Mehta, D., Helmons, R., 2023. Mining of deep-seabed nodules using a Coandă-effect-based collector. Results Eng. 17, 100852.

Alhaddad, S., Suleman, M., Kirichek, A., Chassagne, C., 2024. Experimental investigation of cohesive soil erosion and suspension caused by a Coandă-effect-based polymetallic-nodule collector. Results Eng. 22, 102231.

Amudha, K., Bhattacharya, S., Sharma, R., Gopkumar, K., Kumar, D., Ramadass, G., 2024. Influence of flow area zone and vertical lift motion of polymetallic nodules in hydraulic collecting. Ocean Eng. 294, 116745.

Boetius, A., Haeckel, M., 2018. Mind the seafloor. Science 359 (6371), 34–36.

Cho, S.-g., Park, S., Oh, J., Min, C., Kim, H., Hong, S., Jang, J., Lee, T.H., 2019. Design optimization of deep-seabed pilot miner system with coupled relations between constraints. J. Terramechanics 83, 25–34.

Coughtrie, A., Borman, D., Sleigh, P., 2013. Effects of turbulence modelling on prediction of flow characteristics in a bench-scale anaerobic gas-lift digester. Bioresour. Technol. 138, 297–306.

Elerian, M., Alhaddad, S., Helmons, R., van Rhee, C., 2021. Near-field analysis of turbidity flows generated by polymetallic nodule mining tools. Mining 1 (3), 251–278.

Hao, M., di Mare, L., 2023. Scaling and similarity laws in three-dimensional wall jets. Phys. Fluids 35 (7).

Hu, J., Zhao, G., Xiao, L., Liu, M., 2020. Experimental investigation on characteristics of flow field in 'Suck-up-based' and 'Coandă-Effect-based' nodule pick-up devices. In: ISOPE International Ocean and Polar Engineering Conference. ISOPE, pp. ISOPE–I.

Jia, H., Yang, J., Su, X., 2024. Numerical study on coarse granular flow and performance characteristics of the Coandă effect-based collector for deep sea mining. Appl. Ocean Res. 148, 104033.

Jia, H., Yang, J., Su, X., Wang, Y., Wu, K., 2023. Flow characteristics and hydraulic lift of Coandă effect-based pick-up method for polymetallic nodule. Coatings 13 (2), 271.

Jia, H., Yang, J., Su, X., Xia, Q., Wu, K., 2022. Theoretical prediction on hydraulic lift of a Coandă effect-based mining collector for manganese nodule. Energies 15 (17), 6345.

Kim, M., Kim, H.D., Yeom, E., Kim, K.C., 2018. Flow characteristics of three-dimensional curved wall jets on a cylinder. J. Fluids Eng. 140 (4), 041201.

Lande, A.M., 2021. Complex Mesh Generation with Openfoam. University of South-Eastern Norway.

Lee, M., Hong, S., Choi, J., Kim, H., Yeu, T., Min, C., Cho, S., Lee, T., 2013. Design optimization of a hydraulic deep-sea manganese pick-up device using Coanda effect. In: Proceedings of the KSME Fall Annual Meeting, vol. 12, pp. 1660–1665.

Li, Y., Han, Z., Li, Z., 2024. Numerical simulation and experimental study of a deep-sea polymetallic nodule collector based on the Coanda effect. Minerals 14 (9), 915.

Li, L.-X., Xu, H.-Y., Pei, Z., 2023. Effect of secondary-jet on supersonic Coanda jet. Proc. Inst. Mech. Eng. Part G: J. Aerosp. Eng. 237 (9), 2125–2138.

Li, Y., Zhao, G., Xiao, L., 2025. Experimental investigation on sediment erosion and diffusion characteristics during Coandă-effect-based nodule collection. J. Offshore Mech. Arct. Eng. 147 (4), 041301.

Mao, J., Si, J.-H., Li, G., Wang, X., 2024. Comparison of flow characteristics of plane jet impingement on a solid plate and on a sand bed. Phys. Fluids 36 (3).

Menter, F.R., 1994. Two-equation eddy-viscosity turbulence models for engineering applications. AIAA J. 32 (8), 1598–1605.

Michelsen, B., Strobl, D.-I.S., Pöschel, T., 2012. Validation of Dune Simulations using OpenFOAM (Ph.D. thesis). Friedrich-Alexander-Universität Erlangen-Nürnberg (FAU).

Min, K.-S., Shim, J.-Y., Hong, S., Choi, J.-S., Amann, H., 1997. Conceplual design of a hybrid pick-up device for deep ocean mining. In: ISOPE Ocean Mining and Gas Hydrates Symposium. ISOPE, ISOPE–M.

Pan, Y., Geng, Z., Yuan, H., Zhai, S., Huo, F., 2024. Numerical simulation and flow field analysis of porous water jet nozzle based on fluent. Appl. Sci. 14 (16), 7075.

Peacock, T., Ouillon, R., 2023. The fluid mechanics of deep-sea mining. Annu. Rev. Fluid Mech. 55 (1), 403–430.

Rodman, L.C., Wood, N., Roberts, L., 1989. Experimental investigation of straight and curved annular wall jets. AIAA J. 27 (8), 1059–1067.

Spalart, P.R., Watmuff, J.H., 1993. Experimental and numerical study of a turbulent boundary layer with pressure gradients. J. Fluid Mech. 249, 337–371.

Stoffers, H., Devolder, B., Ramos, P., Heiler, J., 2024. The seafloor nodule collector: Best available techniques and future developments. In: Offshore Technology Conference. OTC, D021S023R003.

Suleman, M., 2023. Cohesive Sediment Erosion Induced By Coandă-Effect-Based Polymetallic-Nodule Collector (Master's thesis). Delft University of Technology, Netherlands, Delft, Netherlands.

Toro, N., Robles, P., Jeldres, R.I., 2020. Seabed mineral resources, an alternative for the future of renewable energy: A critical review. Ore Geol. Rev. 126, 103699.

Wilcox, D.C., et al., 1998. Turbulence Modeling for CFD, vol. 2, DCW industries La Canada, CA.

Wu, Z., Zhang, X., Jin, S., Liu, J., Liu, X., Li, L., Chen, F., Chen, X., Wei, J., Li, H., 2025. Analysis of sediment disturbance and plume dispersion characteristics induced by deep-sea polymetallic nodule hydraulic collectors. Appl. Ocean Res. 156, 104462.

Yue, Z., Zhao, G., Liu, M., Xiao, L., 2021a. Experimental and numerical methods for obtaining flow field formed by hydraulic nodule pick-up devices. Int. J. Offshore Polar Eng. 31 (03), 378–381.

Yue, Z., Zhao, G., Xiao, L., Liu, M., 2021. Comparative study on collection performance of three nodule collection methods in seawater and sediment-seawater mixture. Appl. Ocean Res. 110, 102606.

Zhang, Q., Chen, X., Luan, L., Sha, F., Liu, X., 2024. Technology and equipment of deep-sea mining: State of the art and perspectives. Earth Energy Sci..

Zhang, B., Zhao, G., Xiao, L., Xu, L., 2024. Geometry optimization of wall-jet collection device: A study of flow-field dynamics and particle motion. Phys. Fluids 36 (8).

Zhao, G., Xiao, L., Hu, J., Liu, M., Peng, T., 2021. Fluid flow and particle motion behaviors during seabed nodule pickup: An experimental study. Int. J. Offshore Polar Eng. 31 (02), 210–219.